Cryo-EM structure of the mitochondrial protein-import channel TOM complex at near-atomic resolution

Kyle Tucker [1] and Eunyong Park [1,2]*

Nearly all mitochondrial proteins are encoded by the nuclear genome and imported into mitochondria after synthesis on cytosolic ribosomes. These precursor proteins are translocated into mitochondria by the TOM complex, a protein-conducting channel in the mitochondrial outer membrane. We have determined high-resolution cryo-EM structures of the core TOM complex from *Saccharomyces cerevisiae* in dimeric and tetrameric forms. Dimeric TOM consists of two copies each of five proteins arranged in two-fold symmetry: pore-forming β-barrel protein Tom40 and four auxiliary α-helical transmembrane proteins. The pore of each Tom40 has an overall negatively charged inner surface attributed to multiple functionally important acidic patches. The tetrameric complex is essentially a dimer of dimeric TOM, which may be capable of forming higher-order oligomers. Our study reveals the detailed molecular organization of the TOM complex and provides new insights about the mechanism of protein translocation into mitochondria.

Mitochondria are double-membrane-bound organelles that perform oxidative phosphorylation and other essential cellular functions in eukaryotic cells. There are ~1,000–1,500 mitochondrial proteins, and the vast majority (~99%) are synthesized by cytosolic ribosomes, initially as precursor proteins that are then imported into mitochondria[1–3]. Multiple protein complexes within the organelle mediate membrane translocation and sorting of these precursor polypeptides into four distinct compartments: the outer membrane, the inner membrane, the intermembrane space (IMS), and the matrix. The general import pore in the outer membrane is formed by the TOM complex (translocase of the outer membrane), which is responsible for initial translocation of over 90% of mitochondrial precursor proteins from the cytosol to the IMS.

Studies of the TOM complex of fungal cells have established that it consists of seven transmembrane proteins: Tom40, Tom22, Tom5, Tom6, and Tom7, as well as Tom70 and Tom20 (ref. [4,5]). The first five proteins form a stable complex, referred to as the core TOM complex, and the latter two proteins readily dissociate from the core complex upon isolation in detergent[6,7]. Various analyses have indicated that the detergent-solubilized TOM complex has an apparent molecular mass of ~400–600 kDa and contains multiple copies of each Tom subunit[6–10]. The translocation pore through which precursor polypeptides must pass is formed by Tom40 (ref. [5,11–13]), a β-barrel protein structurally related to the voltage-dependent anion-selective channel VDAC, a major mitochondrial porin[14,15]. The other Tom proteins are associated with Tom40 by their single α-helical transmembrane segments (TMs). Although functions of the α-helical Tom subunits are relatively poorly defined, they have been suggested to act as receptors for precursor proteins[16–20], binding sites for other factors[20,21], and/or escorts that promote assembly and stability of the TOM complex[6,10,22,23].

Current evidence indicates that translocation is a sequential process in which a precursor protein is first recruited by the cytosolic receptor domains of Tom70, Tom20, and Tom22, then threaded into the pore of Tom40, and finally handed over to the translocase of the inner membrane (TIM) complexes or IMS-resident chaperones (review in ref. [2]). However, the underlying mechanism by which the TOM complex enables these events has been unclear. In particular, how the Tom40 channel interacts with mitochondrial targeting motifs within precursor proteins is poorly understood[11,24–26]. The majority of matrix-targeted proteins (~60–70% of mitochondrial precursor proteins) contain a short N-terminal cleavable sequence, termed the presequence, which typically forms a positively charged amphipathic α-helix. The amphipathic nature of the presequence is likely to be important for interaction with the Tom40 pore for initial threading. Recently, a cryo-EM structure of the dimeric core TOM complex from *Neurospora crassa* was reported[27], but its relatively low resolution (~7 Å) precluded building of an atomic model and thus offered only limited insight about the pore structure and the translocation mechanism. Additionally, the oligomeric architecture of the TOM complex is a puzzle. The *N. crassa* structure represents a dimeric complex in which two identical pores are symmetrically arranged. However, based on previous low-resolution EM and cross-linking analyses, it has been generally thought that the TOM complex is rather dynamic and that the mature form is a trimer[5,13,28,29]. The nature of the different oligomeric states remains unclear.

Here we describe near-atomic resolution structures of the core TOM complex from *S. cerevisiae*, determined using cryo-EM: a dimeric structure at 3.1-Å resolution and a tetrameric structure at 4.1-Å resolution. A stable form of the complex is a dimer consisting of two copies each of Tom40, Tom22, Tom5, Tom6, and Tom7 arranged in twofold symmetry. Surface electrostatics calculations show that Tom40 forms a pore with a highly negatively charged surface, which may attract positively charged polypeptides, such as presequences, to initiate translocation. Indeed, neutralization of negatively charged patches in the pore markedly impaired the function of the TOM complex. The tetrameric structure shows that the dimeric TOM complex can further associate into larger oligomers by lateral stacking.

¹Department of Molecular and Cell Biology, University of California, Berkeley, Berkeley, CA, USA. ²California Institute for Quantitative Biosciences, University of California, Berkeley, Berkeley, CA, USA. *e-mail: eunyong_park@berkeley.edu
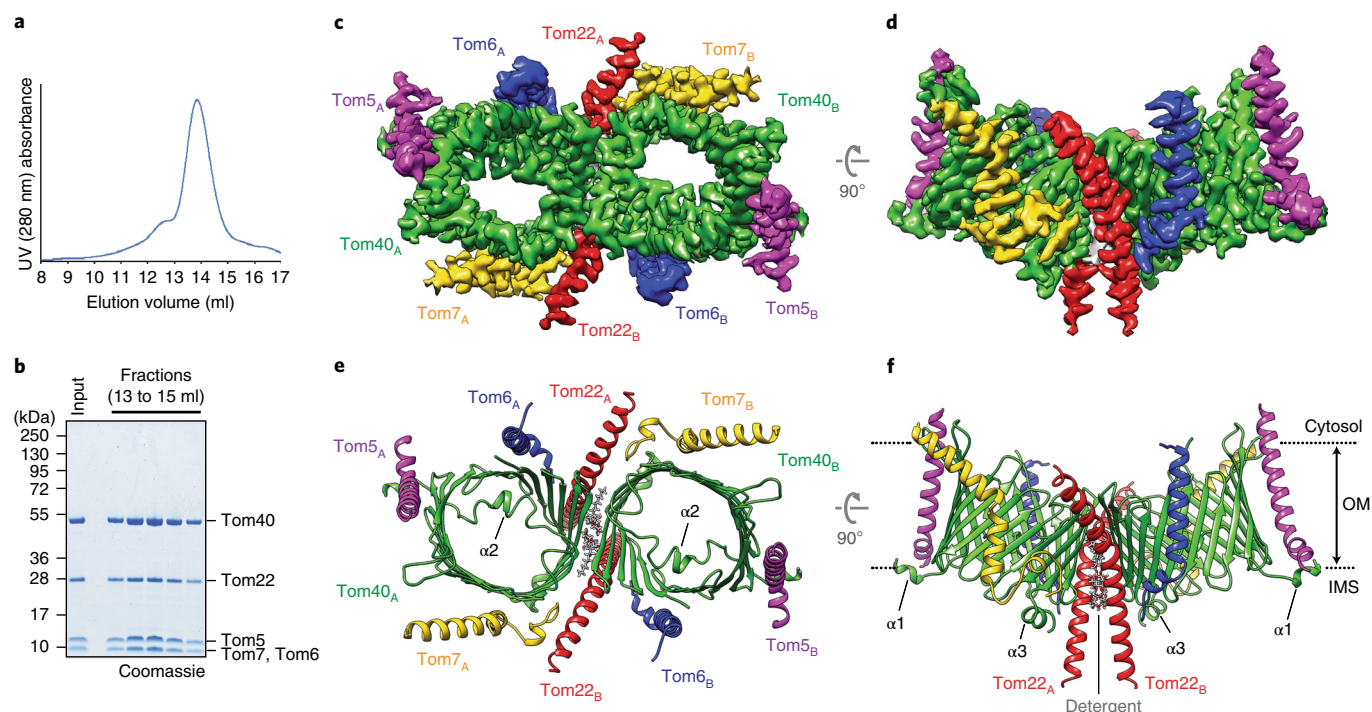
Fig. 1 | Structure of the dimeric core TOM complex from *S. cerevisiae*. a, SEC (Superose 6) profile of the affinity purified yeast TOM complex.
b, Coomassie-stained SDS gel of peak fractions from Superose 6 (**a**). **c,d**, A 3.1-Å-resolution cryo-EM reconstruction of the dimeric TOM complex.
Tom subunits from each asymmetric unit are indicated by subscripts A and B. Shown are views from the cytosol (**c**) and along the membrane plane (**d**).
e,f, Atomic model of the TOM complex in ribbon representation. Two DDM detergent molecules between the Tom40 subunits are represented in sticks.
Three α-helical segments (α1, α2, and α3) of Tom40 are indicated. Dotted lines (in **f**), approximate outer membrane (OM) boundaries.

Results

Cryo-EM analysis of a dimeric TOM complex from yeast. To enable efficient structural analysis, we first developed a new approach to overexpress and purify the *S. cerevisiae* TOM complex. All Tom subunits, except for the weakly associated Tom70 (ref. [9,29]), were expressed in yeast cells from an inducible promoter. The complex was then isolated via affinity purification, utilizing His- and Strep-tags attached to Tom22 and Tom40, respectively. The complex was initially extracted with lauryl maltose neopentyl glycol (LMNG) detergent but was exchanged into dodecyl maltoside (DDM) during affinity purification, because free LMNG micelles often interfere with efficient single-particle cryo-EM analysis[30]. The TOM complex purified by this method was eluted in size-exclusion chromatography (SEC) as a largely monodisperse peak containing Tom40 and other Tom subunits but not Tom20 (Fig. 1a,b). The absence of Tom20 in the sample is likely because of its low-affinity association with the core complex[6,9].

To determine the structure of the TOM complex, we used single-particle cryo-EM analysis (Table 1 and Extended Data Fig. 1). Two- and three-dimensional classifications of particle images showed that the complex is predominantly a dimer (Extended Data Fig. 1a,c), closely resembling the previously reported *N. crassa* structure[27]. After excluding empty detergent micelle and low-quality particles, ~70% of particle images (160,577 out of 243,227) were used for the final 3D reconstruction of the dimeric TOM complex at 3.1-Å resolution with *C*2 symmetry imposed (Fig. 1c,d and Extended Data Fig. 1). Without imposing symmetry, the map was refined to slightly lower resolution (3.2 Å) and manifested no noticeable differences from the symmetrically refined reconstruction (cross-correlation = 0.99; data not shown), indicating that the dimer is highly symmetric. We note that the sample for this dimeric TOM structure additionally included a synthetic presequence peptide. However, the features of this peptide were not sufficiently resolved

in our density map and therefore will not be further discussed. A separate map reconstructed at 3.5-Å resolution from a smaller data set without added presequence peptides showed an essentially identical structure (map cross-correlation = 0.98; data not shown). For the sake of more-accurate modeling, we used the 3.1-Å-resolution map in this study.

Overall structure of the dimeric TOM complex. The near-atomic resolution density map enabled us to build an accurate de novo model of the TOM complex (Fig. 1e,f). A local resolution estimate indicates that a large portion of the complex, especially the Tom40 subunit, is at ~3.0-Å resolution or better (Extended Data Fig. 2a). The map resolves not only individual β-strands of Tom40 but also almost all side chains (Extended Data Fig. 2c). Distal segments of Tom22 and small Tom subunits, however, remain poorly resolved, likely due to intrinsic flexibility. Notably, our subunit assignment agrees with the previous assignment of the *N. crassa* structure[27], which was largely based on cross-linking data[13].

Each monomeric unit of the TOM complex contains a single copy of Tom40, Tom22, Tom5, Tom6, and Tom7, with each Tom40 forming a separate pore for polypeptide passage (Fig. 1c–f). The new structure confirms that the Tom40 barrel consists of 19 β-strands (β1–19) arranged in an antiparallel fashion, except for β1 and β19, which are parallel. Tom40 also has three short α-helical segments, α1 and α2 in the N-terminal segment and α3 near the C terminus. α1 resides on the IMS side, lying flat on the membrane surface as an amphipathic helix. Following α1, a segment containing α2 spans the interior of the Tom40 barrel, as noted previously[13,27]. The structural features of 19 β-strands and an N-terminal segment within the pore closely resemble the structure of VDAC, despite low (~15%) sequence identity[31] (Extended Data Fig. 2d). Although not resolved at high resolution, the ~14-amino-acid-long C-terminal tail of Tom40 following α3 seems directed from IMS into the pore

Table 1 | Cryo-EM data collection, refinement and validation statistics

	Dimeric TOM complex (EMDB-20728) (PDB 6UCU)	Tetrameric TOM complex (EMDB-20729) (PDB 6UCV)
Data collection and processing		
Magnification	43,478×	43,478×
Voltage (kV)	300 kV	300 kV
Electron exposure (e⁻/Å²)	61	43.9
Defocus range (μm)	−0.8 to −2.5	−0.9 to −3.0
Pixel size (Å)	1.15	1.15
Symmetry imposed	C2	C1
Initial particle images (no.)	460,148	173,511
Final particle images (no.)	160,577	104,905
Map resolution (Å)	3.06	4.12
FSC threshold	(0.143)	(0.143)
Map resolution range (Å)	2.6–8.5	3.4–15
Refinement		
Initial model used (PDB code)	De novo	Dimeric complex (6UCU)
Model resolution (Å)	3.06	4.12
FSC threshold	(0.143)	(0.143)
Map sharpening B factor (Å²)	−60	−60
Model composition		
Nonhydrogen atoms	8,414	15,103
Protein residues	7,438	15,011
Ligands	976	92
B factors (Å²)		
Protein	59.81	125.97
Ligand	58.05	71.71
R.m.s. deviations		
Bond lengths (Å)	0.006	0.004
Bond angles (°)	0.955	0.825
Validation		
MolProbity score	1.24	1.34
Clashscore	3.02	3.97
Poor rotamers (%)	0.12	0.00
Ramachandran plot		
Favored (%)	97.22	97.16
Allowed (%)	2.78	2.84
Disallowed (%)	0.00	0.00

of Tom40 and loosely associated with a hydrophobic patch (referred to as HP3; described below) of the pore lining (Extended Data Fig. 2e). Interestingly, the same feature has also been noted with the *N. crassa* structure, despite poor sequence conservation at this region among different species. It is possible that the C-terminal tail may act as an autoinhibitory element that would release from the pore upon insertion of a precursor protein.

At the dimeric interface, the two Tom40 subunits directly contact each other on the cytosolic side by hydrophobic side chains in β1–β19–β18 (Fig. 1c–f and Extended Data Fig. 3a–c). However, a gap opens toward the IMS between the two Tom40 barrels, which are

tilted away from each other by ~40° (Fig. 1g). In our structure, this gap is filled by two DDM molecules and two Tom22 TMs wedged into the interface (Fig. 1c–f and Extended Data Fig. 3c–e). In the native membrane, a phospholipid would occupy this gap in place of detergent, with its head group phosphate positioned to interact with the highly conserved Arg330 of Tom40 (Extended Data Fig. 2c).

Tom22 contains an unusually long (~45 amino acid) α-helix, the middle portion (roughly positions 100–118) of which spans the membrane (Fig. 1f). The helix is longbow-shaped, because of a kink formed by Pro112 (Fig. 2a), a residue that has been reported to be important for mitochondrial targeting of Tom22 and stability of the TOM complex[13,32]. The helix extends at least 22 Å out from the membrane into the IMS, which may function as a binding site for presequences[33] or the TIM complex[34]. On the opposite cytosolic side, the Tom22 helix becomes amphipathic, lying flat on the membrane surface. Preceding the helix, the cytosolic segment (positions 1–88) of Tom22 is invisible, likely due to its flexibility. The function of this region has been suggested to be a docking site for Tom20 and Tom70 (ref. [35,36]) and/or a presequence receptor[19,37]. The mechanism for the latter is unclear, because the domain appears to be directed away from the Tom40 pores. The other three small Tom subunits, Tom5, Tom6, and Tom7, are peripherally bound to Tom40 by interactions with different regions of Tom40 (Fig. 1c–f).

Interactions between β-barrel and α-helical Tom subunits. The TOM complex represents a rare example of a complex consisting of both β-barrel and α-helical types of integral membrane proteins; thus, our structure offers a unique opportunity to examine interactions between the two types of membrane proteins. The structure shows that association between Tom40 and the α-helical Tom subunits is mainly mediated by hydrophobic interactions in conjunction with high surface complementarity between transmembrane domains (Fig. 2a–d and Extended Data Fig. 3d–h). Additionally, several polar interactions were noticed near the membrane boundaries. Conservation of these polar interactions across fungal species suggests that they may play an important role in increasing specificity and affinity of subunit interactions (Supplementary Table 1). Indeed, mutation of Arg261 or Trp243 of Tom40, which interact with Tom6 in our structure, has been shown to decrease the stability of TOM, similar to a Tom6 knockout[38,39].

Our structure also reveals an unusual topology of Tom7, in which its partially unstructured, hook-shaped C-terminal segment spans the IMS leaflet of the outer membrane (Fig. 2d). An unstructured polypeptide in the lipid membrane is rare, because unpaired hydrogen-bond donors and acceptors of the peptide backbone would be energetically unfavorable. In the TOM complex, this issue seems to be overcome by hydrogen bonding between backbone carbonyl oxygen atoms of Tom7 and lipid-facing side chain nitrogen atoms of conserved Lys90 and His102 of Tom40. To test the importance of this interaction, we performed a complementation assay. Previously, it has been shown that deletion of both Tom7 and Tom20 exhibits synthetic lethality[40]. Consistent with this, in the wild-type Tom40 background, exogenously expressed Tom7 rescued growth defects caused by chromosomal deletion of Tom7 and depletion of Tom20 (Fig. 2e). By contrast, with K90A H102A mutant Tom40, no such rescue was seen, likely because Tom7 cannot bind to the mutant Tom40. Instead, expression of Tom7 showed a dominant-negative phenotype in the mutant Tom40 background. Although the exact mechanism is unclear, this finding suggests that unassociated Tom7 exerts a toxic effect. To further verify a loss of the physical interaction between Tom7 and K90A H102A Tom40, we performed purification of the K90A H102A mutant TOM complex using the same procedure as for the wild-type complex. Consistent with the growth complementation experiments, Tom7 was not co-isolated (Fig. 2f). Interestingly, the amounts of copurified Tom6 and Tom22 were also reduced, and the complex seemed to be largely dissociated into
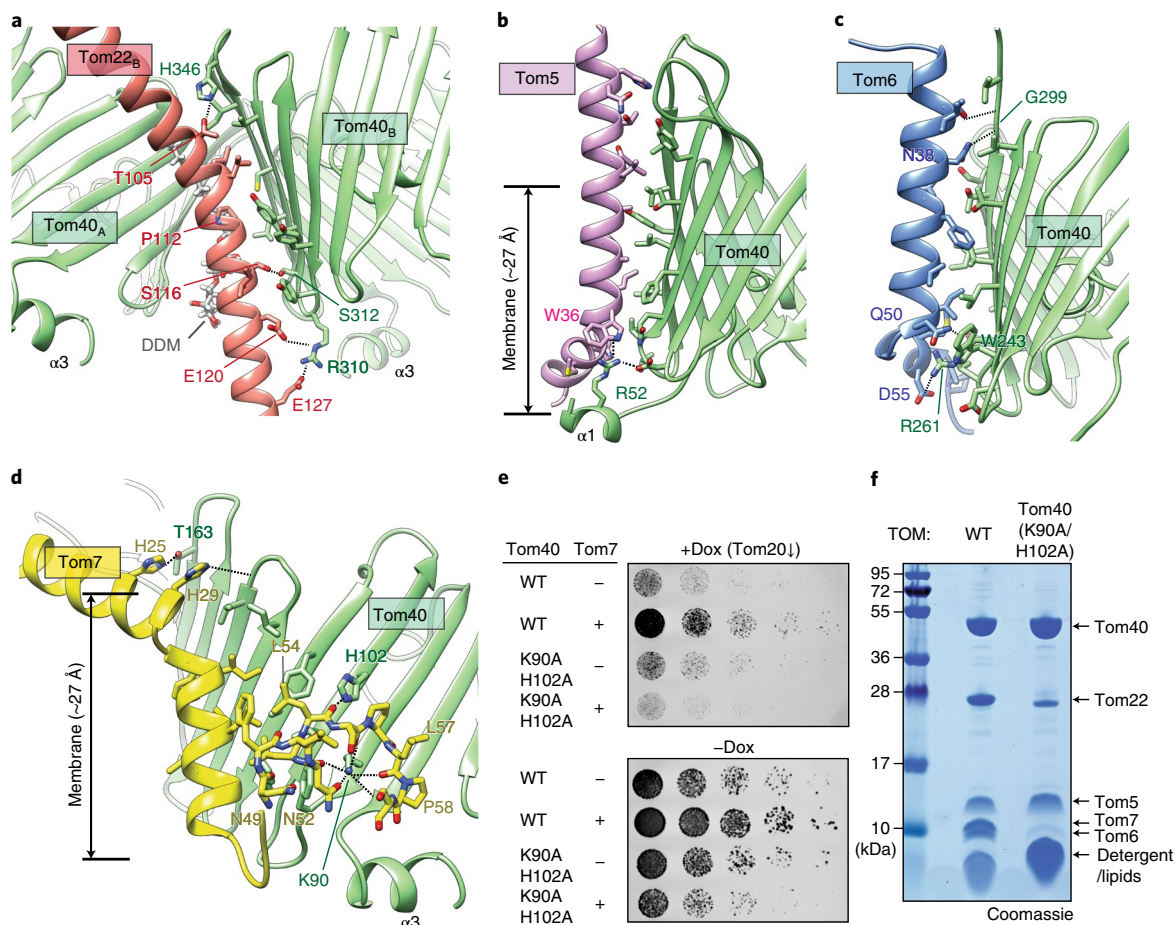
Fig. 2 | Intersubunit contacts between Tom40 and α-helical Tom subunits. a, Interactions between Tom40 and Tom22 within the same monomeric unit. The polar interactions are indicated by black dotted lines. Side views are shown. **b–d,** Interactions of Tom40 with Tom5 (**b**), Tom6 (**c**), and Tom7 (**d**). Note that in **d,** N49–L54 of Tom7 is an α-helix. **e,** Growth complementation of a *tom7Δ* yeast strain with a Tom7-expressing plasmid (tested in a YPD medium containing 2% glucose). Where indicated, endogenous Tom20 was depleted with doxycycline (+Dox), and Tom40 contains K90A and H102A mutations. **f,** Purified TOM complex containing K90A and H102A mutations on Tom40. The experiments in **e** and **f** were repeated twice with similar results. WT, wild type.

monomers (Extended Data Fig. 3i), suggesting additional defects in assembly or stability of the complex[23].

Pore structure of Tom40 and implications for protein translocation mechanism. To gain insight into the protein translocation mechanism by TOM, we examined the translocation pathway in Tom40. Although the Tom40 β-barrel has relatively large (~30 Å by ~25 Å) oval-shaped openings on both the cytosolic and IMS sides, the pore is substantially constricted (~19 Å by ~13 Å) halfway across the membrane by the α2 segment (Fig. 1c,e). Still, the pore would snugly fit one or perhaps two α-helices along the vertical translocation axis. Given the considerable contacts with β7–β19 of Tom40, the α2 segment appears to be a stationary feature of the pore. We also speculate that the Tom40 barrel would be unlikely to open laterally toward the lipid phase, as proposed for BamA and Sam50, which mediate membrane insertion of β-barrel proteins[41–43]. The only separable β-strand pair, β1-β19 would be energetically costly to open, because it is sealed by approximately ten hydrogen bonds and buried at the dimerization interface. Together, these findings suggest that Tom40 is a static pore for polypeptide passage.

To understand how Tom40 may interact with translocating polypeptides, we evaluated surface properties of its pore (Fig. 3 and Extended Data Fig. 4). Surface electrostatic analysis indicates that the pore has an overall negative potential, mainly attributed to multiple acidic patches (referred to as APs 1–3) on the pore lining

(Fig. 3a–d and Extended Data Fig. 4a–d). A similar, overall negative potential is anticipated for Tom40 from other fungal species, based on homology modeling (Fig. 3i and Extended Data Fig. 5). This explains why Tom40 was selective for cations when ion conduction was measured by electrophysiology[11,44]. The negative electrostatic potential likely promotes protein translocation by attracting positively charged amino acids in polypeptides, such as inner membrane proteins and presequences of matrix-targeted preproteins, both of which are often basic[45]. Interestingly, the potential seems to be more negative toward the IMS side (Fig. 3i), which may promote polypeptide movement toward IMS. The pore-lining surfaces also contain hydrophobic patches (HPs; Fig. 3e–h), which may interact with precursor proteins to facilitate translocation.

To test the functional importance of these patches, we examined cell growth defects associated with their mutations on the basis that Tom40's protein translocation function is essential for cell viability (Fig. 3j and Extended Data Fig. 4h). When we mutated the conserved and most prominent acidic patch AP2 by replacing five glutamate and aspartate residues with asparagine ('complete' mutant), a substantial growth retardation was observed. The defect seems largely due to the charge neutralization of AP2 residues on the IMS side (AP2_{IMS}). When an additional positive charge (E329R) was introduced at AP2_{IMS}, growth was further reduced. Complete neutralization of AP3, which is localized near the IMS opening next to AP2_{IMS}, also led to similar growth defects. Together, these
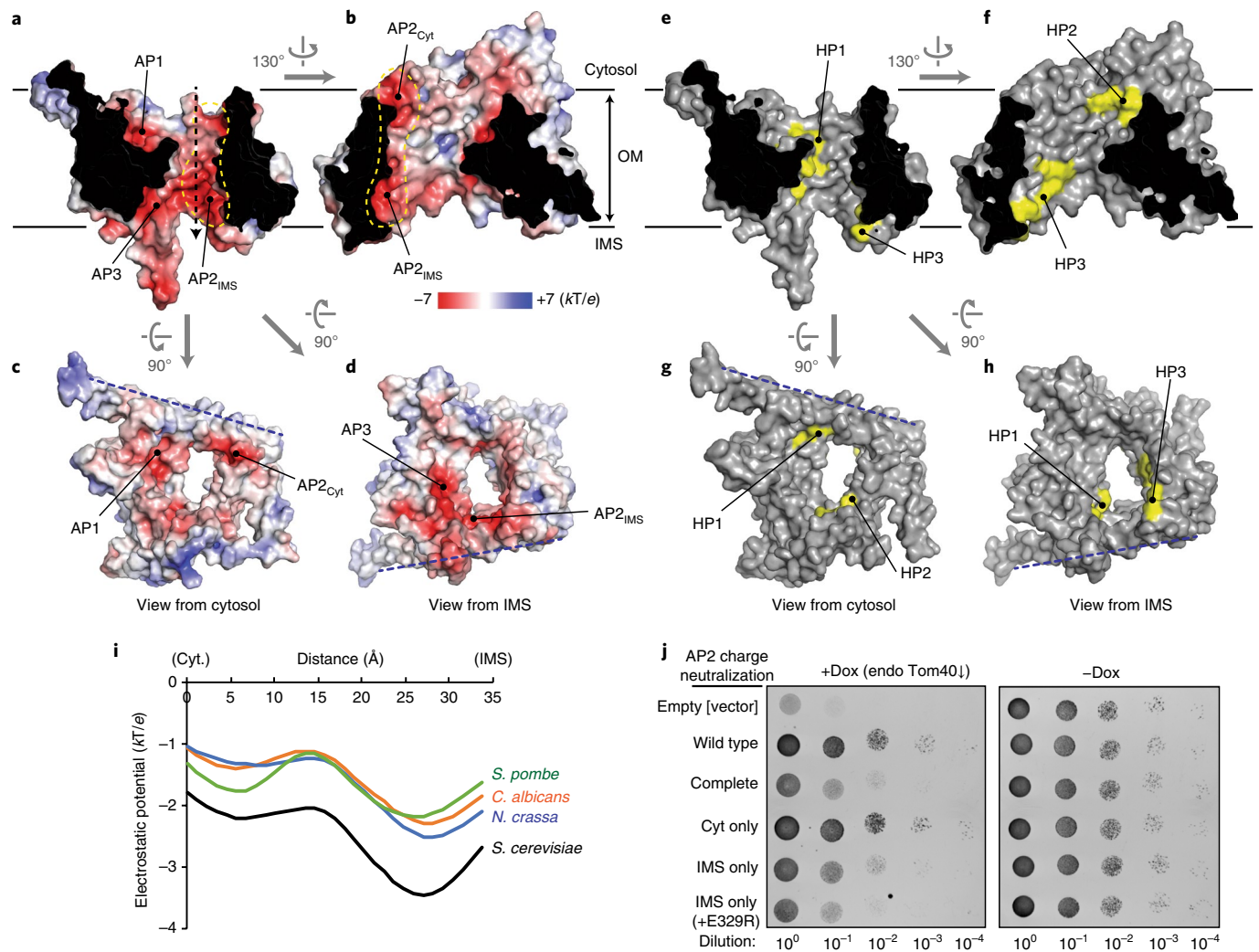
Fig. 3 | Pore architecture of Tom40. a–d, Surface electrostatics of the TOM complex shown as a heat map on a solvent-accessible surface representation. For simplicity, only one monomeric unit is shown (the dimer interface is indicated by a blue dashed line in **c** and **d**). Shown are cutaway side views (**a,b**) and views from the cytosol (**c**) and IMS (**d**). Acidic patches are referred to as AP1, AP2 (also outlined by yellow dash line), and AP3. Black dashed arrow, pore axis. **e–h,** As in **a–d**, but showing hydrophobic patches (HPs) in yellow. **i,** Electrostatic potential along the pore axis (black dashed arrow in **a**). After calculating electrostatic potential using homology models for indicated species, values along the pore axis were extracted and plotted. **j,** Yeast cells expressing an indicated Tom40 mutant from a CEN plasmid were serially diluted and spotted on SC (−Leu) plates containing 2% glucose. In these strains, the presence of doxycycline (+Dox) represses expression of chromosomal Tom40. IMS only, D87N E329N E360N; Cyt only, D132N D134N; complete, a combination of IMS and Cyt. The experiment in **j** was repeated three times with similar results.

results suggest the importance of a negative electric potential at the IMS side of the pore. We also observed impaired growth phenotypes when we mutated either HP2 or HP3 (Extended Data Fig. 4h). Incomplete growth inhibition by the mutation of individual patches might be due to their functional redundancy.

Assessment of oligomeric structure of TOM. The oligomeric nature of the TOM complex is a long-standing puzzle. Our structure, as well as the *N. crassa* structure[27], suggests that the dimer is a stable configuration and likely to be translocation competent. However, previous low-resolution EM and cross-linking studies have proposed that the mature or holo-TOM complex is a trimer[5,13,28,29]. It remains unclear whether and how the TOM complex switches between different oligomeric states.

During our purification experiments, we made a surprising observation that under a more-gentle detergent condition, the TOM complex can be purified as a larger species than a dimer (Fig. 4 and

Extended Data Fig. 6). Although exchange of LMNG into DDM during affinity purification resulted almost exclusively in dimers that migrated as an ~500-kDa species (Fig. 4a), delayed exchange into DDM at the last SEC step produced an additional peak appearing at a higher molecular size (~1 MDa) (Fig. 4b). When DDM was substituted by glyco-diosgenin (GDN), a digitonin-like detergent that is generally considered to be more gentle than DDM, the complex eluted mostly in the 1-MDa peak (Fig. 4c). The sample also seemed to contain even larger species, as some Tom proteins eluted earlier. Importantly, SDS-PAGE analysis of peak fractions showed no changes in subunit composition (Extended Data Fig. 6f), indicating that the two peaks simply differ in their oligomeric states. Similar high-molecular-weight species of the TOM complex were observed when crude cell or mitochondrial extracts were analyzed via SEC under gentle-detergent conditions (Fig. 4d,e).

Because many previous studies evaluating the TOM complex assembly have used blue native PAGE (BN-PAGE) analysis[6,9,10,19,22,35],
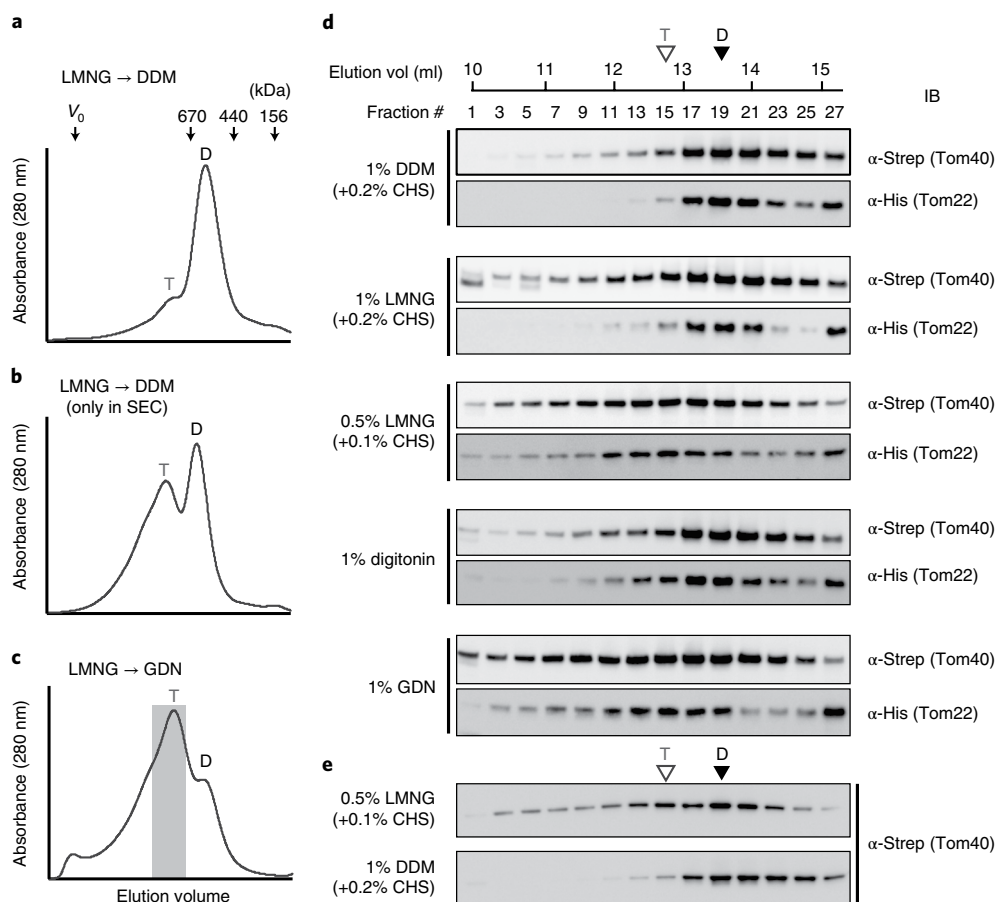
Fig. 4 | Analysis of oligomeric states of the TOM complex. a–c, SEC elution profiles of the TOM complex in different detergent conditions (details in Extended Data Fig. 6a–e). V_0, void volume. In **c**, fractions in gray were used for cryo-EM analysis in Fig. 5 and Extended Data Fig. 7. Two distinct peaks are marked as T and D. **d**, Cells overexpressing the TOM complex (cultured in a medium containing 2% ethanol and 3% glycerol as the carbon source) were lysed in indicated detergent condition, and the lysates were injected onto a Superose 6 column. The fractions were analyzed via SDS-PAGE and immunoblotting (IB). The column was equilibrated with buffer containing the same detergent used for membrane solubilization at a low concentration, as described in Methods. Approximate peak positions are marked with T and D based on the UV absorbance profiles shown in **a–c** (Extended Data Fig. 6b–e). Note that the anti-Strep-tag antibody appears to have a substantially lower detection limit (higher sensitivity) than the anti-His-tag antibody. **e**, As in **d**, but using solubilized mitochondrial fractions with endogenous (chromosomal) Tom40 tagged with a Strep-tag. The experiments in **d** and **e** were repeated twice with similar results. Source data for **d** and **e** are available with the paper online.

we also subjected the extracts to BN-PAGE in addition to SEC analysis (Extended Data Fig. 6g). This comparison, together with the new cryo-EM structure, suggest that the previously reported 400-kDa band in BN-PAGE corresponds to the dimeric complex. A discrepancy between the nominal size of dimeric TOM (~160 kDa) and its apparent size (400–500 kDa) in SEC and BN-PAGE seems to originate from the complex's flat structure with hollow pores and a large detergent micelle around it. Unlike SEC analysis, BN-PAGE did not show prominent higher-oligomer species, perhaps due to dissociation into dimers in the harsh conditions of BN-PAGE[7].

Cryo-EM structure of the tetrameric TOM complex. To understand how the larger species are organized, we analyzed the 1-MDa peak fractions using cryo-EM (Fig. 5a–c and Extended Data Fig. 7). As expected from the SEC analysis, particles on micrographs were much larger than those seen with the dimer sample (Extended Data Fig. 7b). Two- and three-dimensional classifications of particle images showed a striking tetrameric arrangement of the pores (Extended Data Fig. 7a,c). We also noticed that micrographs often showed particles larger than the dimensions of the tetramer, indicating that the sample included oligomers larger than tetramers (Extended Data Fig. 7g), consistent with the SEC profile. Notably,

a minor 3D class showed three pores (Extended Data Fig. 7a; class 3), reminiscent of trimers seen in low-resolution EM studies[5,28,29]. This 'trimer' class appears to be similar to the tetramer class, lacking one monomeric unit.

The tetramer structure determined at 4.1-Å resolution reveals that it is essentially a dimer of two dimeric TOM complexes (referred to as A–B and C–D), which are arranged in a staggered parallel fashion that would allow further assembly into larger oligomers (Fig. 5a–b and Extended Data Fig. 7). There are only a few structural differences between the dimeric complex and dimers in the tetrameric complex, as two copies of atomic models for the dimer could be fitted into the EM map, essentially as rigid bodies. The dimer-to-dimer contact is contributed by two Tom6 subunits ($Tom6_B$ and $Tom6_C$) as well as Tom22 and Tom5 (referred to as $Tom22_B$ and $Tom5_C$) (Fig. 5a,b and Extended Data Fig. 8). Particularly, each of two Tom6 subunits at the interface interact with Tom40 from the other dimeric complex, where its flexible N-terminal segment (residues 1–25) appears to be directed to the Tom40's barrel interior next to β11 and near HP2 (Fig. 5b and Extended Data Fig. 9a). This interaction readily explains the result of previous in organello cross-linking experiments that Tom6 can cross-link to two opposite sides of the Tom40 barrel[13,46]. Lastly, it is noteworthy that the tetramer is not completely
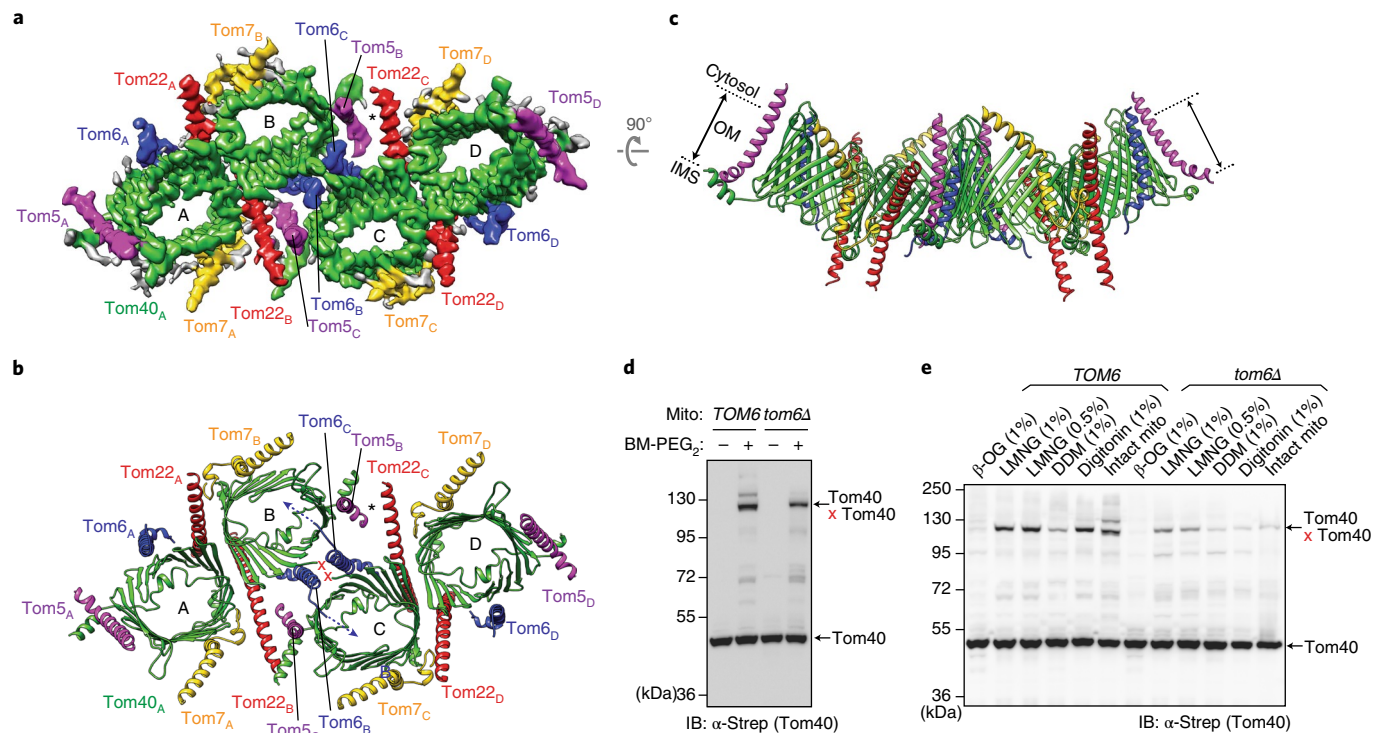
Fig. 5 | Cryo-EM structure of the tetrameric TOM complex. a–c, Cryo-EM reconstruction (**a**) and atomic model (**b,c**) of the tetrameric TOM complex. Four monomeric units are indicated by A, B, C, and D. Shown are views from the cytosol (**a,b**) and along the membrane plane (**c**). Asterisk, gap between Tom5$_B$ and Tom22$_C$. Red 'X' shows the approximate position of the cysteine introduced for cross-linking experiments (287C). **d,** Cross-linking between two Tom40 copies (at the endogenous level) in isolated mitochondria by bismaleimido-diethyleneglycol (BM-PEG$_2$). Where indicated, chromosomal Tom6 was deleted (*tom6Δ*). Cells were grown in a YPD medium. **e,** As in **d**, but cross-linking was performed after solubilization of mitochondrial membranes with indicated detergents. The experiments in **d** and **e** were repeated twice with similar results. Source data for **d** and **e** are available with the paper online.

symmetric, such that a gap exists at one of the two Tom22-Tom5 contacts (Fig. 5a,b and Extended Data Fig. 8a–c). Furthermore, there is a considerable gap (~7 Å in width) along the dimer-dimer interface at the IMS leaflet of the membrane (Extended Data Fig. 8i), creating a concave curvature to the cytosolic side (Fig. 5c). In the cryo-EM map, the gaps are filled by weak density features, which should be detergent and/or lipid molecules (Extended Data Fig. 8h and data not shown). It is possible that in the native membrane, the gap is closed such that the complex lies relatively flat in the membrane. Looking from the IMS, protein surfaces in the interface are roughly complementary between the two TOM dimers to accommodate such a closure (Extended Data Fig. 8i). Nevertheless, the relatively loose interface explains why tetramers easily dissociate into dimers by excess detergent and suggests that the TOM oligomers undergo a dynamic equilibrium in the native membrane.

Examination of mitochondrial detergent extracts by SEC showed the presence of higher-order TOM oligomers at the endogenous level (Fig. 4e). To test whether their oligomeric configuration is consistent with that of the tetramer structure, we performed cross-linking experiments by introducing a cysteine to the L14–15 loop of Tom40. Although the L14–15 loop is not fully resolved in our cryo-EM maps, it is located near the dimer-dimer interface of the tetramer such that the distance between two sulfhydryl groups of introduced cysteines may become close enough (<14 Å) to be cross-linked by a bismaleimide-PEG$_2$ (Fig. 5b and Extended Data Fig. 9a); however, cross-linking would not be achievable between the two Tom40 molecules within a dimeric complex (the distance is ~60 Å). Indeed, Tom40 could be efficiently cross-linked via cysteines at position 287 after being extracted with LMNG or digitonin, as well as in intact mitochondria, where tetramers are expected (Fig. 5d,e and Extended Data Fig. 9b–d). By contrast, little or no

cross-linking was obtained when the complex was extracted with DDM or octyl glucoside, conditions in which the complex largely dissociates into dimers or monomers[12]. While these results do not address the previously proposed trimeric TOM complex, as a high-resolution structure of such a configuration is not available, they are consistent with tetrameric and higher oligomeric configurations observed in our structural analysis. Lastly, we tested effects of Tom6 deletion on the oligomerization of the TOM complex. Although lack of Tom6 did not prevent formation of higher oligomers in both cross-linking and SEC experiments (Figs. 4e, 5d,e, and Extended Data Fig. 9e), it substantially decreased the cross-linking efficiency, suggesting that Tom6 promotes formation of oligomers in the configuration revealed by our structure.

Discussion

Our high-resolution structures of the yeast TOM complex offer new mechanistic insights into how Tom40 mediates translocation of precursor proteins. While precursor polypeptides are first recognized by the cytosolic domains of Tom20 and Tom70, they need to be threaded into the pore of Tom40. Because there is no external energy input (that is, ATP or membrane potential) involved, this early step of translocation must be driven solely by the affinity of precursor proteins toward the pore interior. Our structural and functional analyses suggest that electrostatic interactions between the Tom40 pore and the precursor protein play an important role in this process (Fig. 6). Particularly, in the cases of presequence-containing proteins, the positively charged presequence may be first attracted into the overall negatively charged Tom40 pore and then drawn toward the IMS by interaction with acidic patches on the IMS side. This mode of interaction may provide not only a driving force for presequence insertion into the pore but also an additional
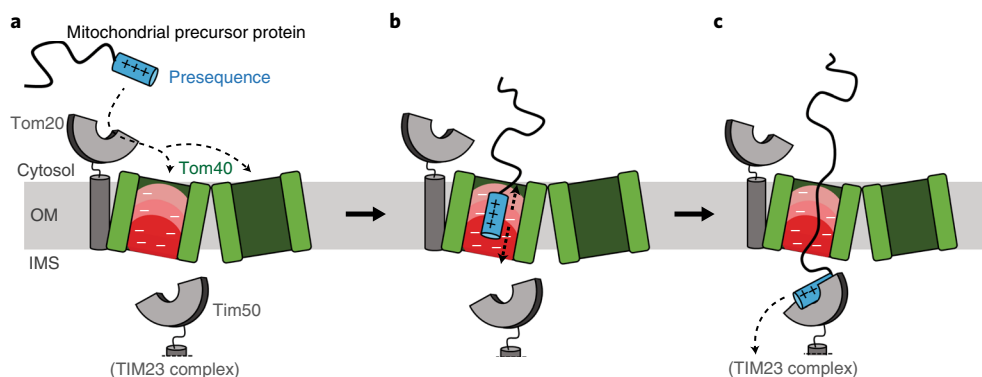
Fig. 6 | Model for presequence engagement with the TOM complex. a, The presequence is initially recruited to Tom20 by hydrophobic interactions with the cytosolic domain of Tom20. The presequence is attracted into one of two pores of the TOM complex by the negative electrostatic potential of the pores. **b**, The presequence inserts into the pore close to the IMS by electrostatic interactions. Thermal motions would allow the presequence to move vertically along the pore. **c**, Once exposed to the IMS, the presequence binds to the soluble domain of Tim50, which would further hand it over to the TIM23 complex.

'filter' for increased targeting specificity, as initial recognition of presequences by Tom20 is mediated by hydrophobic interactions[18]. It remains to be elucidated how the presequence moves out from the pore interior into the IMS. This would likely require thermal (Brownian) motion of the precursor protein, as well as some movement of the C-terminal tail of Tom40. Once exposed in the IMS, the presequence might be captured by Tim50 of the TIM23 complex, which has been shown to interact with presequences[47], and would thus be prevented from backsliding.

A highly unexpected finding was that the TOM complex can form a tetramer and larger oligomers. While the dimeric form is likely a functional unit, its clustering into larger oligomers might fine-tune the protein import activity. Unlike previous low-resolution EM studies[5,28,29], we did not observe a symmetrical trimer class throughout our cryo-EM analyses. It is possible that the difference might be because our samples lacked Tom20, which has been proposed to mediate trimerization of Tom40 (ref. [28]), and, therefore, our study does not directly argue against the trimer model. In light of high-resolution structures, future studies will be necessary to re-evaluate the trimeric configuration and understand how Tom20 would mediate formation of trimers despite its seemingly weak association to the complex. It also remains to be elucidated what functional state the tetrameric and larger assemblies represent. One possibility is that the TOM complexes cluster into larger assemblies to increase import efficiency, potentially advantageous for the cotranslational import, where multiple precursor molecules would be produced on a polysome[48]. Lastly, our study shows that formation of tetramers and higher-order oligomers is facilitated by Tom6, which coincides well with its proposed function in stabilizing the TOM complex[6,49]. It has been shown previously that phosphorylation of Tom6's N-terminal tail (Ser16) increases the steady-state levels of Tom6 and the TOM complex, as well as overall mitochondrial protein import[49]. Such modifications on Tom subunits could regulate the dynamics of TOM oligomerization. Our work provides a framework for further investigations to understand the structure, dynamics, and functions of the high-order TOM complex assemblies we have discovered.

Online content

Any methods, additional references, Nature Research reporting summaries, source data, extended data, supplementary information, acknowledgements, peer review information; details of author contributions and competing interests; and statements of data and code availability are available at https://doi.org/10.1038/s41594-019-0339-2.

References

1. Wiedemann, N. & Pfanner, N. Mitochondrial machineries for protein import and assembly. *Annu. Rev. Biochem.* **86**, 685–714 (2017).
2. Chacinska, A., Koehler, C. M., Milenkovic, D., Lithgow, T. & Pfanner, N. Importing mitochondrial proteins: machineries and mechanisms. *Cell* **138**, 628–644 (2009).
3. Neupert, W. & Herrmann, J. M. Translocation of proteins into mitochondria. *Annu. Rev. Biochem.* **76**, 723–749 (2007).
4. Kiebler, M. et al. Identification of a mitochondrial receptor complex required for recognition and membrane insertion of precursor proteins. *Nature* **348**, 610–616 (1990).
5. Kunkele, K. P. et al. The preprotein translocation channel of the outer membrane of mitochondria. *Cell* **93**, 1009–1019 (1998).
6. Dekker, P. J. et al. Preprotein translocase of the outer mitochondrial membrane: molecular dissection and assembly of the general import pore complex. *Mol. Cell Biol.* **18**, 6515–6524 (1998).
7. Ahting, U. et al. The TOM core complex: the general protein import pore of the outer membrane of mitochondria. *J. Cell Biol.* **147**, 959–968 (1999).
8. Rapaport, D. et al. Dynamics of the TOM complex of mitochondria during binding and translocation of preproteins. *Mol. Cell Biol.* **18**, 5256–5262 (1998).
9. Meisinger, C. et al. Protein import channel of the outer mitochondrial membrane: a highly stable Tom40-Tom22 core structure differentially interacts with preproteins, small Tom proteins, and import receptors. *Mol. Cell Biol.* **21**, 2337–2348 (2001).
10. Schmitt, S. et al. Role of Tom5 in maintaining the structural stability of the TOM complex of mitochondria. *J. Biol. Chem.* **280**, 14499–14506 (2005).
11. Hill, K. et al. Tom40 forms the hydrophilic channel of the mitochondrial import pore for preproteins. *Nature* **395**, 516–521 (1998); comment **395**, 439−440.
12. Ahting, U. et al. Tom40, the pore-forming component of the protein-conducting TOM channel in the outer membrane of mitochondria. *J. Cell Biol.* **153**, 1151–1160 (2001).
13. Shiota, T. et al. Molecular architecture of the active mitochondrial protein gate. *Science* **349**, 1544–1548 (2015).
14. Zeth, K. Structure and evolution of mitochondrial outer membrane proteins of beta-barrel topology. *Biochim. Biophys. Acta* **1797**, 1292–1299 (2010).
15. Lackey, S. W. et al. Evidence supporting the 19 beta-strand model for Tom40 from cysteine scanning and protease site accessibility studies. *J. Biol. Chem.* **289**, 21640–21650 (2014).
16. Bolliger, L., Junne, T., Schatz, G. & Lithgow, T. Acidic receptor domains on both sides of the outer membrane mediate translocation of precursor proteins into yeast mitochondria. *EMBO J.* **14**, 6318–6326 (1995).
17. Dietmeier, K. et al. Tom5 functionally links mitochondrial preprotein receptors to the general import pore. *Nature* **388**, 195–200 (1997).
18. Abe, Y. et al. Structural basis of presequence recognition by the mitochondrial protein import receptor Tom20. *Cell* **100**, 551–560 (2000).
19. Yamano, K. et al. Tom20 and Tom22 share the common signal recognition pathway in mitochondrial protein import. *J. Biol. Chem.* **283**, 3799–3807 (2008).

20. Yamamoto, H. et al. Roles of Tom70 in import of presequence-containing mitochondrial proteins. *J. Biol. Chem.* **284**, 31635–31646 (2009).

21. Qiu, J. et al. Coupling of mitochondrial import and export translocases by receptor-mediated supercomplex formation. *Cell* **154**, 596–608 (2013).

22. Sherman, E. L., Go, N. E. & Nargang, F. E. Functions of the small proteins in the TOM complex of *Neurospora crassa*. *Mol. Biol. Cell* **16**, 4172–4182 (2005).

23. Becker, T. et al. Biogenesis of mitochondria: dual role of Tom7 in modulating assembly of the preprotein translocase of the outer membrane. *J. Mol. Biol.* **405**, 113–124 (2011).

24. Rapaport, D., Neupert, W. & Lill, R. Mitochondrial protein import. Tom40 plays a major role in targeting and translocation of preproteins by forming a specific binding site for the presequence. *J Biol. Chem.* **272**, 18725–18731 (1997).

25. Melin, J. et al. Presequence recognition by the Tom40 channel contributes to precursor translocation into the mitochondrial matrix. *Mol. Cell Biol.* **34**, 3473–3485 (2014).

26. Vogtle, F. N. et al. Global analysis of the mitochondrial N-proteome identifies a processing peptidase critical for protein stability. *Cell* **139**, 428–439 (2009).

27. Bausewein, T. et al. Cryo-EM Structure of the TOM core complex from *Neurospora crassa*. *Cell* **170**, 693–700.e7 (2017).

28. Model, K. et al. Protein translocase of the outer mitochondrial membrane: role of import receptors in the structural organization of the TOM complex. *J. Mol. Biol.* **316**, 657–666 (2002).

29. Model, K., Meisinger, C. & Kuhlbrandt, W. Cryo-electron microscopy structure of a yeast mitochondrial preprotein translocase. *J. Mol. Biol.* **383**, 1049–1057 (2008).

30. Hauer, F. et al. GraDeR: Membrane protein complex preparation for single-particle cryo-EM. *Structure* **23**, 1769–1775 (2015).

31. Ujwal, R. et al. The crystal structure of mouse VDAC1 at 2.3 Å resolution reveals mechanistic insights into metabolite gating. *Proc. Natl Acad. Sci. USA* **105**, 17742–17747 (2008).

32. Allen, R., Egan, B., Gabriel, K., Beilharz, T. & Lithgow, T. A conserved proline residue is present in the transmembrane-spanning domain of Tom7 and other tail-anchored protein subunits of the TOM translocase. *FEBS Lett.* **514**, 347–350 (2002).

33. Moczko, M. et al. The intermembrane space domain of mitochondrial Tom22 functions as a trans binding site for preproteins with N-terminal targeting sequences. *Mol. Cell Biol.* **17**, 6574–6584 (1997).

34. Albrecht, R. et al. The Tim21 binding domain connects the preprotein translocases of both mitochondrial membranes. *EMBO Rep.* **7**, 1233–1238 (2006).

35. van Wilpe, S. et al. Tom22 is a multifunctional organizer of the mitochondrial preprotein translocase. *Nature* **401**, 485–489 (1999).

36. Shiota, T., Mabuchi, H., Tanaka-Yamano, S., Yamano, K. & Endo, T. In vivo protein-interaction mapping of a mitochondrial translocator protein Tom22 at work. *Proc. Natl Acad. Sci. USA* **108**, 15179–15183 (2011).

37. Brix, J., Rudiger, S., Bukau, B., Schneider-Mergener, J. & Pfanner, N. Distribution of binding sequences for the mitochondrial import receptors Tom20, Tom22, and Tom70 in a presequence-carrying preprotein and a non-cleavable preprotein. *J. Biol. Chem.* **274**, 16522–16530 (1999).

38. Sherman, E. L., Taylor, R. D., Go, N. E. & Nargang, F. E. Effect of mutations in Tom40 on stability of the translocase of the outer mitochondrial membrane (TOM) complex, assembly of Tom40, and import of mitochondrial preproteins. *J. Biol. Chem.* **281**, 22554–22565 (2006).

39. Gabriel, K., Egan, B. & Lithgow, T. Tom40, the import channel of the mitochondrial outer membrane, plays an active role in sorting imported proteins. *EMBO J.* **22**, 2380–2386 (2003).

40. Honlinger, A. et al. Tom7 modulates the dynamics of the mitochondrial outer membrane translocase and plays a pathway-related role in protein import. *EMBO J.* **15**, 2125–2137 (1996).

41. Bakelar, J., Buchanan, S. K. & Noinaj, N. The structure of the beta-barrel assembly machinery complex. *Science* **351**, 180–186 (2016).

42. Gu, Y. et al. Structural basis of outer membrane protein insertion by the BAM complex. *Nature* **531**, 64–69 (2016).

43. Hohr, A. I. C. et al. Membrane protein insertion through a mitochondrial β-barrel gate. *Science* **359**, eaah6834 (2018).

44. Kunkele, K. P. et al. The isolated complex of the translocase of the outer membrane of mitochondria. Characterization of the cation-selective and voltage-gated preprotein-conducting pore. *J. Biol. Chem.* **273**, 31032–31039 (1998).

45. Da Cruz, S. et al. Proteomic analysis of the mouse liver mitochondrial inner membrane. *J. Biol. Chem.* **278**, 41566–41571 (2003).

46. Sakaue, H. et al. Porin associates with Tom22 to regulate the mitochondrial protein gate assembly. *Mol. Cell* **73**, 1044–1055.e8 (2019).

47. Schulz, C. et al. Tim50's presequence receptor domain is essential for signal driven transport across the TIM23 complex. *J. Cell Biol.* **195**, 643–656 (2011).

48. Williams, C. C., Jan, C. H. & Weissman, J. S. Targeting and plasticity of mitochondrial proteins revealed by proximity-specific ribosome profiling. *Science* **346**, 748–751 (2014).

49. Harbauer, A. B. et al. Mitochondria. Cell cycle-dependent regulation of mitochondrial preprotein translocase. *Science* **346**, 1109–1113 (2014).

Methods

Constructions of plasmid and yeast strains. To generate an *S. cerevisiae* strain overexpressing the TOM complex components from an inducible *GAL1* promoter, we used the Yeast Tool Kit (YTK) and Golden Gate assembly[50]. We first amplified coding sequences (CDS) for Tom40, Tom22, Tom20, Tom 7, Tom6, and Tom5 via PCR using genomic DNA of *S. cerevisiae* BY4741 as a template and cloned them individually into the pYTK1 entry plasmid. To enable affinity purification of the Tom complex, a Strep-tag (GGWSHPQFEK) and a His-tag (GGHHHHHHHH) were introduced before the stop codons of Tom40 and Tom22, respectively. The cloned Tom subunits were combined with YTK parts to generate individual expression cassettes, each containing the *GAL1* promoter (YTK30), CDS of a Tom subunit, and the *ENO1* terminator (YTK61). In the case of the purification in Fig. 2f and Extended Data Fig. 3i, Tom40 CDS included K90A and H102A mutations, which were introduced via site-directed mutagenesis. The six Tom expression cassettes were assembled into a single multigene plasmid, concatenating them in the order of Tom40-Tom22-Tom20-Tom7-Tom6-Tom5. The plasmid also contained a nourseothricin resistance marker (YTK78) for selection and *URA3* homology arms (YTK92 and YTK86) for chromosomal integration. The resulting assembly was introduced to the yMLT62 yeast strain (a gift from J. Thorner) by a standard lithium acetate transformation method after linearizing the plasmid with the NotI endonuclease. The colonies were selected on a YPD agar plate containing 100 µg/ml nourseothricin, and chromosomal integration was confirmed by PCR. The yMLT62 strain (BY4741 *leu2::pACT1-GEV::HIS3MX*) contains the chimeric transcriptional activator Gal4dbd.ER.VP16 (GEV; ref. [51]) integrated to the *LEU2* locus, which induces the transcription by the *GAL1* promoter upon addition of β-estradiol to the growth medium.

To generate strains expressing Tom40 under the native promoter, we first used PCR to amplify the endogenous Tom40 gene region (of BY4741), including the 329-bp segment upstream of the start codon and the 381-bp segment downstream of the stop codon. This fragment was then inserted into a homemade yeast CEN/ARS plasmid constructed with YTK (used parts: pYTK84, pYTK8, pYTK47, pYTK73, pYTK75, and pYTK81). The plasmid contained a *LEU2* marker for selection. For immunodetection, we attached a Strep-tag to the C-terminus of Tom40 using PCR (the resulting plasmid is referred to as pe112-Tom40_Strep). Where indicated, other mutations were also introduced by PCR. In some experiments, plasmids (pe115-Tom40_Strep or pe115-Tom40_His) contained a nourseothricin resistance marker (from pYTK78) instead of the *LEU2* marker. Where a cysteine-free or single-cysteine mutant of Tom40 was used, the endogenous cysteines of Tom40 were mutated to alanine or methionine (C165A/C326A/C341A/C355M).

To replace chromosomal wild-type Tom40 with a cysteine-free or single-cysteine version (287C, 291C, or 293C), we used homologous recombination using a PCR fragment amplified from the Tom40-expressing plasmids (same as pe112-Tom40_Strep except that these constructs have a shorter downstream segment (172 bp instead of 381 bp) following the stop codon of Tom40_Strep). The DNA segment containing a 5′ upstream region of Tom40, the CDS of Tom40, a 3′ downstream region, and the *LEU2* marker was amplified via PCR with a forward primer (CAGGGACATGGGTAAGAACTTG) and a reverse primer (gaccattgtgaa-agtaaggacaaggatatgagacgtatcataactataaacaaggaattcCTGCCTATTTAACGCCAAC; lower case indicates the homologous region to the chromosomal locus). The PCR products were purified and introduced to the yeast strain BY4741 by means of lithium acetate transformation. Colonies were isolated from a synthetic complete agar medium lacking leucine (SC(-Leu)). Colonies with correct double-crossover recombination were screened by PCR of genomic DNA and Sanger sequencing.

A strain expressing Tom20 under a tetracycline-repressible promoter (replacing the native promoter of Tom20) was generated on the R1158 strain (Dharmacon) background, as described previously[52]. Deletion of chromosomal Tom7 (*tom7Δ::HIS3*) was carried out by transformation of a PCR product generated from YTK76 (*HIS3* marker) as a template, a forward primer (agaaactagttccc-tcttatctctcaatatttgccaaaattagctttttaacaaataaaccCTGTGGATAACCGTAGTCG), and a reverse primer (taattcaaaattggaaatatgggcttcctctctcacccaagttgtatcga-actgatgtttGGGCGTTTTTTATTGGTC). Deletion of chromosomal Tom6 (*tom6Δ::URA3*) was performed similarly using pYTK76 (*URA3* marker), a forward primer (ccatgtcctgtaggcttctcaagagaacaaaaacaaaacacagacaaaataa-ttgaaaACTGTGGATAACCGTAGTCG), and a reverse primer (caaaaaccaatatatatac aggtaagtgaaaaaatctcaactatacaagaaccaaccccGGGCGTTTTTTATTGGTC). Deletion was confirmed via PCR of genomic DNA. To introduce a K90A H102A mutation to chromosomal *TOM40*, we used a marker-free CRISPR−Cas9 approach[50], using a sgRNA targeting the 57–64th codons of Tom40 CDS (G CTG GTC AAT CCC GGT ACC GTG G) and a repair DNA containing the K90A H102A mutation and CRISPR-resistant synonymous codons (G TTA GTT AAC CCT GGT ACT GTC G), which were amplified using a pe112-Tom40 template and primers (CAGGGACATGGGTAAGAACTTG; TAAACCTAAAGCTAATTGAGGAG). The successful mutation was confirmed by Sanger sequencing.

Purification of the TOM complex. Yeast cells were grown in YPEG medium (1% yeast extract, 2% peptone, 2% ethanol and 3% glycerol) in shaker flasks at 30 °C. Upon reaching an optical density (OD_600) of ~1.4–2, cells were induced with 50 nM β-estradiol. After 9–10 h of induction, cells were harvested via centrifugation at 5,000 r.p.m. Cell pellets were flash frozen in liquid nitrogen and stored in −80 °C

until use. The TOM complex was purified via tandem affinity purification using His- and Strep-tags, as summarized in Extended Data Fig. 6a. Cells were first lysed by cryomilling at the liquid nitrogen temperature and resuspended in buffer (3× cell pellet volume) containing 50 mM Tris-HCl, pH 8, 200 mM NaCl, 10% glycerol, 20 mM imidazole, and protease inhibitors (5 µg/ml aprotinin, 5 µg/ml leupeptin, 1 µg/ml pepstatin A, and 1 mM PMSF). Then, one cell pellet volume of 5% lauryl maltose neopentyl glycol (LMNG; Anatrace) and 1% cholesteryl hemisuccinate (CHS; Anatrace) was added to solubilize membranes. After a 3-h incubation at 4 °C, the lysate was clarified by ultracentrifugation (Beckman Coulter rotor Type 45Ti) at 125,000g for 1 h. The lysate was incubated by gentle rotation with HisPur cobalt resin (Life Technologies) for 3 h at 4 °C. The beads were then packed in a gravity column and washed with approximately 10 column volumes (CVs) of buffer containing 50 mM Tris-HCl, pH 8, 200 mM NaCl, 0.02% LMNG, 0.004% CHS, 20 mM imidazole, and 10% glycerol. Resin was further washed with an additional 10 CVs of buffer containing 40 mM imidazole and eluted with approximately 6 CVs of buffer containing 180 mM imidazole. The eluate was then mixed with Strep-Tactin Sepharose (IBA Lifesciences) for ~14 h at 4 °C. The beads were packed in a gravity column and washed with approximately 10 CVs of buffer containing 20 mM Tris-HCl, pH 7.5, 100 mM NaCl, 0.03% dodecyl-β-maltoside (DDM; Anatrace), 0.006% CHS, and 1 mM dithiothreitol (DTT). In the case of purification of the tetrameric TOM complex, 0.02% glyco-diosgenin (GDN; Anatrace) was used instead of DDM and CHS. The TOM complex was eluted with buffer containing 3 mM D-desthiobiotin and concentrated using AmiconUltra (100 kDa cut-off, Millipore). The complex was further purified by SEC using a Superose 6 Increase 10/300 GL column (GE Lifesciences) equilibrated with 20 mM Tris-HCl, pH 7.5, 100 mM NaCl, 1 mM DTT, and 0.03% DDM, 0.006% CHS (for the dimeric TOM complex) or 0.02% GDN (for the tetrameric TOM complex). Peak fractions were pooled, concentrated to ~3.5–5 mg/ml using AmiconUltra (100 kDa cut-off; Millipore), and used to prepare cryo-EM grids. For experiments described in Extended Data Fig. 6b–f, essentially the same procedure was employed but with modified detergent conditions as indicated. Purification of the TOM complex containing K90A H102A-mutant Tom40 (Fig. 2f and Extended Data Fig. 3i) were carried out with the same procedure used for purification of the wild-type dimeric TOM complex.

Cryo-EM specimen preparation and data acquisition. Immediately before preparing cryo-EM grids, 3 mM fluorinated Fos-Choline-8 (FFC8; Anatrace) was added to the purified TOM sample. We note that the addition of 3 mM FFC8 did not cause any changes in the SEC profiles of either the dimeric or tetrameric TOM complex, even after a prolonged (~6 h) incubation. To prepare cryo-EM grids, ~3 µl of the sample was applied to a glow-discharged Quantifoil holey carbon grid (R 1.2/1.3 Au, 400 mesh; Quantifoil). Glow discharge was carried out for 20 s in 75% argon and 25% oxygen using a Gatan Solarus plasma cleaner or in air using a PELCO easiGlow glow discharge cleaner. The grid was blotted with Whatman No. 1 filter papers for 3 s at 4 °C and 100% humidity and plunge frozen in liquid-nitrogen-cooled liquid ethane using Vitrobot Mark IV (FEI).

A summary of image acquisition parameters is shown in Table 1. The data sets were collected on a Titan Krios electron microscope (FEI) equipped with a K2 Summit direct electron detector (Gatan) and a GIF Quantum image filter (Gatan). The microscope was operated at an acceleration voltage of 300 kV. Dose-fractionated images were collected in the super-resolution mode with a physical pixel size of 1.15 Å and a GIF slit width of 20 eV, using SerialEM software[53]. The dose rate was 1.22 electrons/Å²/frame, with a frame rate of 0.2 s. For the dimeric complex, the total accumulated dose was 61 electrons/Å² (50 frames), and for the tetrameric TOM complex, it was 48.8 electrons/Å² (40 frames).

Single-particle image analysis of the dimeric TOM complex. A summary of the single-particle analysis procedure is described in Extended Data Fig. 1a. Briefly, RELION3 (ref. [54]) was used for preprocessing of movies, particle picking, and Bayesian particle polishing, and then cryoSPARC v2 (ref. [55]) was used for ab initio reconstruction, 3D classification, and the final 3D reconstruction. First, the movies were imported to RELION3 and corrected for motion using MotionCor2 with 5-by-5 tiling (ref. [56]). During this step, micrographs were 2×-pixel-binned (resulting in a pixel size of 1.15 Å). Micrographs that were not suitable for image analysis (for example, micrographs containing crystalline ice or displaying a large drift) were removed by manual inspection. Defocus parameters were estimated using CTFFIND4 (ref. [57]). Template-based automatic particle picking was performed in RELION3 (460,148 particles from 1,587 movies). The particle templates were generated by 2D classification from Laplacian autopicking on a subset of the data. The particles were extracted from micrographs with a box size of 256 pixels. Reference-free 2D classification (Extended Data Fig. 1c) was performed to remove empty detergent micelles and obvious non-protein particle artifacts, resulting in 290,793 particles. The initial 3D model was generated by cryoSPARC (ab initio reconstruction). The first 3D refinement was carried out by RELION3 using a low-pass-filtered initial model and 290,793 particle images, yielding a 3.8-Å-resolution reconstruction. The particle images were subjected to one round of CTF refinement and Bayesian particle polishing in RELION3. These particles were subjected to a second 3D refinement, which yielded a 3.6-Å-resolution reconstruction. Then, another round of CTF refinement and particle polishing was

performed. The resulting polished particles were imported to cryoSPARC v2 for the subsequent process, as described below.

The imported particles were subjected to 2D classification in cryoSPARC to further discard artifacts and low-quality particles. The resulting 243,227 particles were used to generate four ab initio 3D reconstructions, followed by heterogeneous refinement (3D classification). A total of 179,232 (74%) particles converged to one class (class 3; Extended Data Fig. 1a) leading to a high-resolution reconstruction of the dimeric TOM complex; whereas two low-resolution classes (classes 1 and 2) appeared to have only a single pore, likely corresponding to dissociated monomers. After a second round of 3D classification to further remove low-quality particles, 160,577 particles from class 3 were refined by non-uniform refinement with $C2$ symmetry imposed, yielding the final map at 3.06-Å resolution (based on gold-standard Fourier shell correlation (FSC) and the 0.143 cut-off criterion; Extended Data Fig. 1e). Local resolution was estimated by cryoSPARC using default parameters (Extended Data Fig. 2a).

Single-particle image analysis of the tetrameric TOM complex. Summaries of single-particle image analysis for the tetrameric TOM complexes are shown in Extended Data Fig. 7a. Essentially, motion correction, defocus estimation, particle picking, and particle extraction were performed using Warp (ref. [58]), and the remaining downstream refinement process was carried out using cryoSPARC v2. Movies were corrected for motion with 8-by-8 tiling, and defocus parameters were estimated with 5-by-5 tiling. Original super-resolution micrographs were 2×-pixel-binned. Particles were automatically picked by Warp. Micrographs were manually inspected to remove unsuitable micrographs. Particle images were extracted with a box size of 400 pixels from dose-weighted frames 1–36 (skipping the last 4 frames). Particle images were then imported to cryoSPARC and subjected to one round of reference-free 2D classification to remove empty micelles. Ab initio reconstruction was performed to generate four (for tetrameric TOM) initial 3D models, which were then subjected to a heterogeneous refinement. Approximately 80% of particle images converged into two nearly identical classes (classes 1 and 2) showing high-resolution features. These particle images were used for the final 3D reconstructions by non-uniform refinement in cryoSPARC, yielding maps at resolutions of 4.1 Å. No symmetry ($C1$) was imposed, because the complex was found to be not completely symmetric (imposition of $C2$ symmetry led to artificial distortion of some density features). Local resolution was also estimated by cryoSPARC using default parameters.

Atomic model building. A summary of model refinement and validation is shown in Table 1. The atomic model for dimeric TOM was built de novo using Coot (ref. [59]) and the summed map. In addition to proteins, we also modeled several hydrophobic tails of detergent or lipid (we used DDM as a model). The model was refined in real space using Phenix (ref. [60]) and the summed map with the refinement resolution limit set to 3.1 Å. Different weights were tested using half maps to check whether the used Phenix refinement protocol shows overfitting to the map (Extended Data Fig. 2b; FSC_{work} vs. FSC_{free}). To this end, we chose a weight of 2, which did not separate FSC_{work} and FSC_{free}. We also used restraints for secondary structure. The following segments were not modeled because of poor or invisible density features: N–48, 277–294, and 374–387(C) of Tom40, N–85 and 136–152(C) of Tom22, N–12 and N–26 and 48–50 (C) of Tom6, and N–10 of Tom7.

To build a model for the tetrameric TOM complex, two dimer models were fit into the tetramer map using UCSF Chimera. A few additional residues (α1 of Tom40, 81–89 of Tom22, and 25–26 of Tom6) were built using Coot, because the tetramer map shows extra densities for these segments. Additionally, we modeled 1,2-dimyristoyl-rac-glycero-3-phosphocholine (DMPC) into the density at the Tom40-Tom40 dimer interface (instead of DDM, as in the dimeric TOM complex). The model was then refined against the tetramer map in essentially the same way as that described for the dimeric TOM complex. Structural validation was done using MolProbity (ref. [61]).

Protein electrostatics were calculated using PDB2PQR and the Adaptive Poisson-Boltzmann Solver (www.poissonboltzmann.org; ref. [62]) with monovalent mobile ions (0.1 M for both cation and anion) included in parameters. UCSF Chimera and PyMOL (Schrödinger) were used to prepare structural figures in the paper.

Yeast growth assays. To test functional complementation by mutant Tom40, we used a yeast strain (TH_7610; Dharmacon) from the Yeast Tet-Promoters Hughes Collection, in which the original Tom40 promoter was replaced by a tetracycline promoter (tet_{prom}). The cells were transformed with a CEN/ARS plasmid (pe112-Tom40$_{Strep}$) constitutively expressing wild-type or mutant Tom40$_{Strep}$ under the endogenous promoter and selected on agar plates of a synthetic complete medium containing 2% glucose and lacking leucine (SC(−Leu)). After a 3-d incubation at 30 °C, colonies were isolated. Cells were grown in 3 ml of SC(−Leu) at 30 °C until OD$_{600}$ reached ~0.7–1.5, pelleted, and resuspended in fresh medium at OD$_{600}$ of 1. After tenfold serial dilution, 10 µl was spotted on SC(−Leu) agar plates. Where indicated, 15 µg/ml doxycycline was included in the medium to repress endogenous Tom40 expression. Plates were incubated at 30 °C for ~2–2.5 d before imaging. To test expression of the Tom40 mutants in cells, an equal number (2 ODs) of cells were collected from cultures in SC(−Leu) medium, and proteins were extracted by heating in NaOH/SDS solution. The samples were analyzed by

SDS-PAGE and immunoblotting with anti-Strep (Genscript; A01732) and anti-PGK1 (a gift from J. Thorner) antibodies. Standard enhanced chemiluminescence reagents and a Fujifilm LAS-3000 Imager were used for detection.

For the complementation experiment in Fig. 2e, the yeast strain (R1158 tet$_{prom}$-TOM20::KanMX tom7Δ::HIS3) was transformed with pe115-Tom7, which expresses wild-type Tom7 from the native promoter (the cloned region includes from 262-bp upstream to 209-bp downstream of the Tom7 CDS) or an empty pe115 vector. The transformants were selected on YPD (1% yeast extract, 2% peptone, 2% glucose) agar supplemented with 100 µg/ml nourseothricin. After growth in YPD with 100 µg/ml nourseothricin, cultures were diluted to OD$_{600}$ of 0.1 and further diluted fivefold in serial, and then 10 µl was spotted on YPD/nourseothricin agar plates, which were incubated at 30 °C for ~2 d before imaging. Where indicated, 10 µg/ml doxycycline was included in the medium to deplete Tom20.

Size-exclusion chromatography and blue native PAGE analysis of extracts. Yeast cells were grown in YPEG medium and induced by β-estradiol, as previously stated. Cells from ~10-ml induced culture were pelleted, washed in distilled water, frozen in liquid nitrogen and stored at −80 °C until use. Pelleted cells (~100 mg) were resuspended in 400 µl of lysis buffer containing 50 mM Tris-HCl, pH 7.5, 200 mM NaCl, 1 mM EDTA, 2 mM DTT, and protease inhibitors. Cells were lysed by beating with pre-chilled glass beads (two cycles of 1.5-min beating and 1-min rest). Beads were removed, and the lysate was mixed with detergent (from a 5% stock solution), as indicated. After solubilizing membranes for 1 h at 4 °C, samples were clarified for 1 h at 13,300 r.p.m. and 4 °C. One-hundred microliters of the clarified sample was injected into a Superose 6 column equilibrated with 20 mM Tris-HCl, pH 7.5, 150 mM NaCl, 1 mM EDTA, 1 mM DTT, and a low concentration of detergent used for lysis (that is, 0.03% DDM, 0.006% CHS; 0.02% LMNG, 0.004% CHS; 0.02% GDN; or 0.08% digitonin). Fractions were collected and analyzed by SDS-PAGE and immunoblotting analyses. For immunoblotting, anti-Strep-tag and anti-His-tag (Life Technologies; MA1-21315) monoclonal antibodies were used.

Samples for BN-PAGE were prepared essentially the same way but with a minor modification. The lysis buffer contained 50 mM Tris pH 7.5, 50 mM NaCl, 10% glycerol, 1 mM DTT, and protease inhibitors. Detergent-solubilized lysates were clarified by ultracentrifugation for 30 min at 250,000 g (Beckman TLA-100 rotor) and 4 °C. Coomassie Blue G-250 (prepared as a 5% stock in 0.5 M 6-aminohexanoic acid; 1/4 amount of added detergent by weight) was added to the lysate. BN-PAGE was performed using a 4–16% Novex Native PAGE gel (Life Technologies) according to the manufacturer's instructions.

Where crude mitochondria fractions were used instead of whole cell lysates for SEC analysis (Fig. 4e and Extended Data Fig. 9e), detergents were added directly to mitochondria (400 µg in 100 µL of 10 mM MOPS pH 7.2 and 250 mM sucrose) for 1.5 h on ice with intermittent mixing. After clarification by centrifugation, the sample was injected into a Superose 6 column, and fractions were analyzed as described above.

Tom40-Tom40 cross-linking. A total of 0.2 mM BM-PEG$_2$ was added to 50 µg of crude mitochondria in 50 µl of 10 mM MOPS, pH 7.2, and 250 mM sucrose for 4 min at 23 °C (20-min incubation was used for experiments in Extended Data Fig. 9b,c). Where detergent extracts were used, mitochondria were first solubilized on ice for 1.5 h with indicated detergent (when LMNG or DDM was used, 0.2× CHS was supplemented) before adding bismaleimido-diethyleneglycol (BM-PEG$_2$; Thermo Pierce). Reactions were quenched with the addition of 50 mM DTT (or 20 mM NEM in Extended Data Fig. 9b,c) on ice for 20 min. Proteins were precipitated with 10% TCA, washed with cold acetone, and resuspended in SDS sample buffer prior to SDS-PAGE and immunoblotting. For the immunoprecipitation experiment in Extended Data Fig. 9c, mitochondria were pelleted and solubilized in buffer containing 20 mM Tris-HCl, pH 7.5, 150 mM NaCl, 100 mM β-OG for 1 h on ice after cross-linking with BM-PEG$_2$. The extract was clarified and incubated first with 2 µg anti-Strep antibody (or no antibody in mock) for 2 h at 4 °C and additionally with 25 µl of Protein A beads (Thermo/Pierce) for 2 h. The beads were washed with the solubilization buffer containing 50 mM β-OG, and bound proteins were eluted with SDS sample buffer. The samples were analyzed by SDS-PAGE and immunoblotting using anti-His antibody conjugated to horse radish peroxidase (Proteintech; HRP-66005). For cross-linking after SEC (Extended Data Fig. 9d), ~850 µg of mitochondria was solubilized in 100 µl buffer containing 10 mM MOPS, pH 7.2, 250 mM sucrose, 0.5% LMNG and 0.1% CHS for 1.5 h on ice. The clarified extract was then injected into a Superose 6 column. Fractions were incubated with 0.2 mM BM-PEG$_2$, quenched with 50 mM DTT and analyzed by SDS-PAGE and immunoblotting.

Reporting Summary. Further information on research design is available in the Nature Research Reporting Summary linked to this article.

Data availability

The cryo-EM density maps and atomic model are available through EM DataBank (EMD-20728, EMD-20729) and Protein Data Bank (PDB 6UCU, PDB 6UCV), respectively. Source data for Figs. 4d,e and 5d,e are available with the paper online.

References

50. Lee, M. E., DeLoache, W. C., Cervantes, B. & Dueber, J. E. A highly characterized yeast toolkit for modular, multipart assembly. *ACS Synth. Biol.* **4**, 975–986 (2015).
51. McIsaac, R. et al. Fast-acting and nearly gratuitous induction of gene expression and protein depletion in *Saccharomyces cerevisiae*. *Mol. Biol. Cell* **22**, 4447–4459 (2011).
52. Mnaimneh, S. et al. Exploration of essential gene functions via titratable promoter alleles. *Cell* **118**, 31–44 (2004).
53. Mastronarde, D. N. Automated electron microscope tomography using robust prediction of specimen movements. *J. Struct. Biol.* **152**, 36–51 (2005).
54. Zivanov, J. et al. New tools for automated high-resolution cryo-EM structure determination in RELION-3. *eLife* **7**, e42166 (2018).
55. Punjani, A., Rubinstein, J. L., Fleet, D. J. & Brubaker, M. A. cryoSPARC: algorithms for rapid unsupervised cryo-EM structure determination. *Nat. Methods* **14**, 290–296 (2017).
56. Zheng, S. Q. et al. MotionCor2: anisotropic correction of beam-induced motion for improved cryo-electron microscopy. *Nat. Methods* **14**, 331–332 (2017).
57. Rohou, A. & Grigorieff, N. CTFFIND4: fast and accurate defocus estimation from electron micrographs. *J. Struct. Biol.* **192**, 216–221 (2015).
58. Tegunov, T. C. P. Real-time cryo-EM data pre-processing with Warp. *Nat. Methods* **16**, 1146–1152 (2019).
59. Emsley, P., Lohkamp, B., Scott, W. G. & Cowtan, K. Features and development of Coot. *Acta Crystallogr. D Biol. Crystallogr.* **66**, 486–501 (2010).
60. Afonine, P. V. et al. Real-space refinement in PHENIX for cryo-EM and crystallography. *Acta Crystallogr. D Struct. Biol.* **74**, 531–544 (2018).
61. Chen, V. B. et al. MolProbity: all-atom structure validation for macromolecular crystallography. *Acta Crystallogr. D Biol. Crystallogr.* **66**, 12–21 (2010).
62. Dolinsky, T. J., Nielsen, J. E., McCammon, J. A. & Baker, N. A. PDB2PQR: an automated pipeline for the setup of Poisson-Boltzmann electrostatics calculations. *Nucleic Acids Res.* **32**, W665–W667 (2004).

Author Contributions

E.P. conceived the project. K.T. and E.P. performed experiments. E.P. built the atomic models. K.T. and E.P. interpreted results and wrote the manuscript. E.P. supervised the project.

Competing interests

The authors declare no competing interests.

Additional information

Extended data is available for this paper at https://doi.org/10.1038/s41594-019-0339-2.

Supplementary information is available for this paper at https://doi.org/10.1038/s41594-019-0339-2.

Correspondence and requests for materials should be addressed to E.P.

Peer review information Katarzyna Marcinkiewicz was the primary editor on this article and managed its editorial process and peer review in collaboration with the rest of the editorial team.

Reprints and permissions information is available at www.nature.com/reprints.
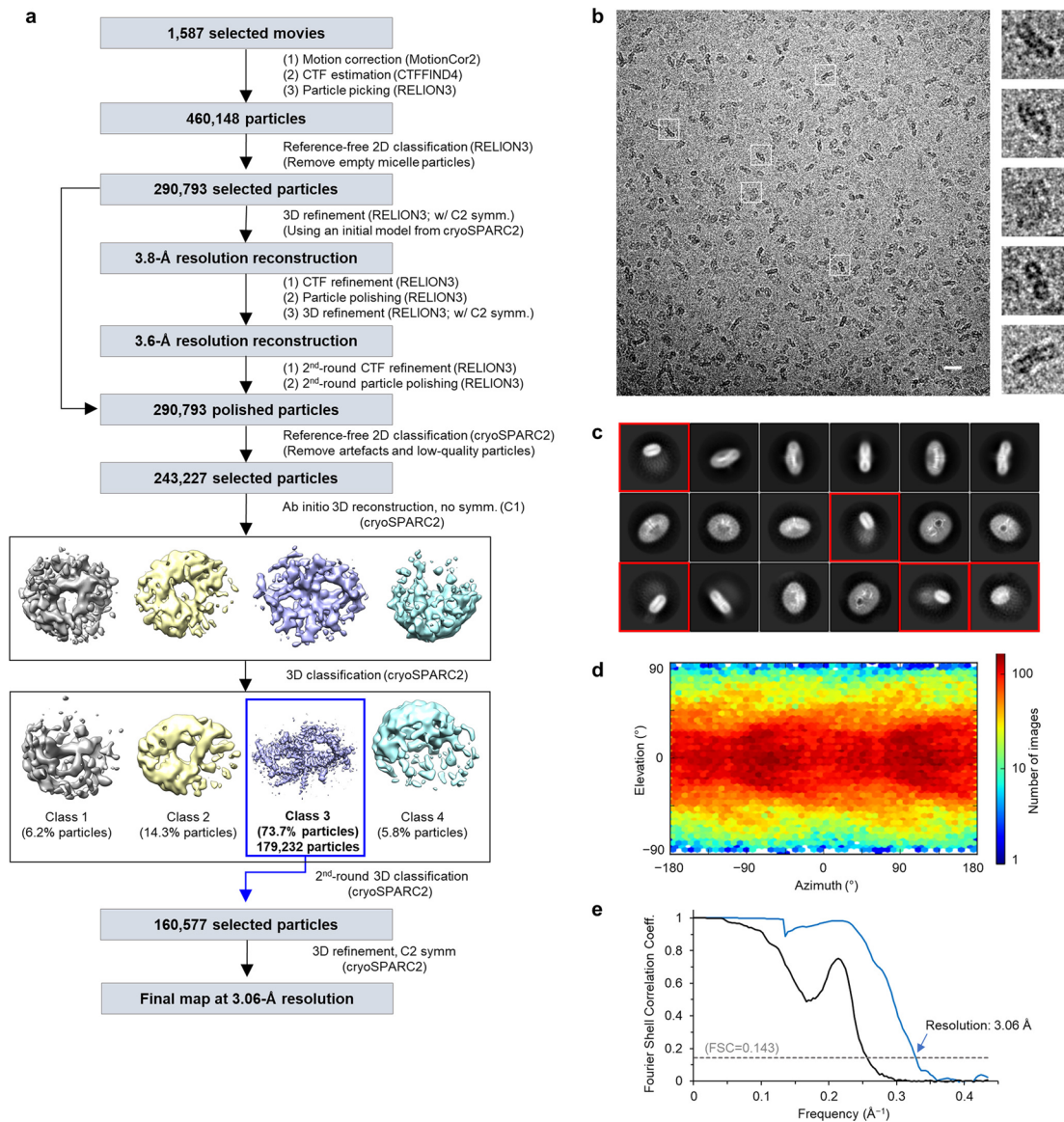
Extended Data Fig. 1 | Single-particle cryo-EM analysis of the dimeric core TOM complex. a, Summary of single-particle image analysis procedure.
b, A representative motion-corrected micrograph. Scale bar, 20 nm. Right panels show magnified images of selected particles outlined with white squares.
The particle image size is 209 Å (width) by 209 Å (height). **c**, Representative class averages from 2D classification by RELION3. The box dimensions are
297 Å (width) by 297 Å (height). Classes in red boxes are likely empty micelles and thus excluded in subsequent analysis. **d**, Heat map showing particle
orientation distribution (produced in the final 3D reconstruction by cryoSPARC2). **e**, Fourier shell correlation (FSC) of two independently refined half maps.
Blue line, corrected masked FSC. Solid black line, unmasked FSC.
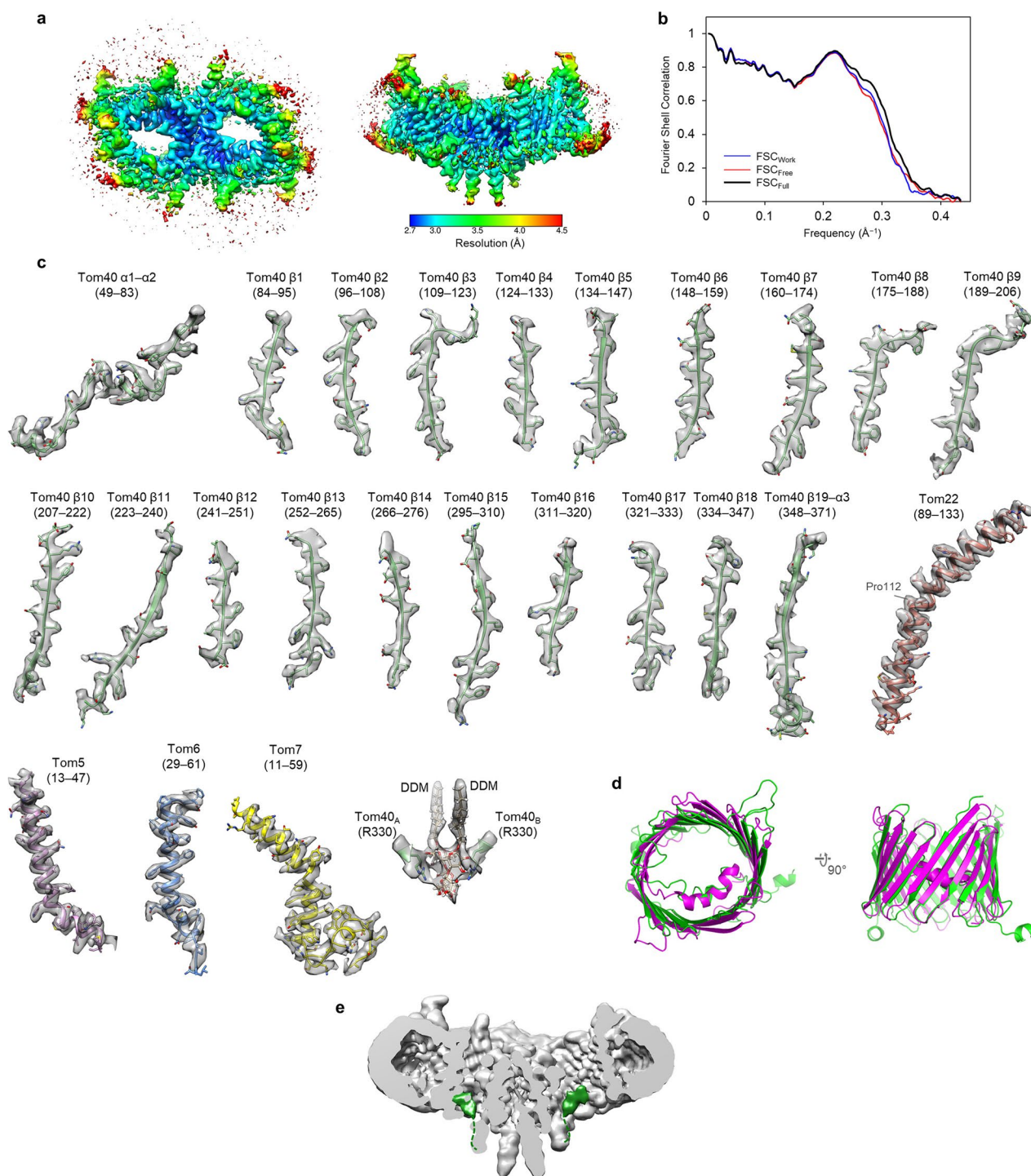
Extended Data Fig. 2 | Cryo-EM map and atomic model quality of the dimeric TOM complex. a, Local resolution represented by a heat map on the density contour (unsharpened, summed map). **b**, FSC between the EM map and the atomic model. Blue curve, FSC_{work} (FSC between half map 1 and a model refined against half map 1). Red curve, FSC_{free} (FSC between half map 2 and the model refined against half map 1). Black curve, FSC_{full} (FSC between the combined map and the final atomic model refined against the combined map. All refinements were performed by Phenix with the same weight. **c**, Examples of the density map and the atomic model for indicated segments. Numbers in the brackets indicate ranges of amino acid residues shown. **d**, Structural comparison of Tom40 and VDAC. Structures of Tom40 (this study; green) and murine VDAC (PDB 3EMN; magenta) are superimposed. Left, view from cytosol. Right, side view. **e**, Density features (green) for the C-terminal tails of Tom40 are shown in a 5-Å low-pass-filtered map. Shown is vertical cross-section along the Tom40 pores. A weak connection (not shown) between the density in green and α3 of Tom40 is indicated by a dashed line.
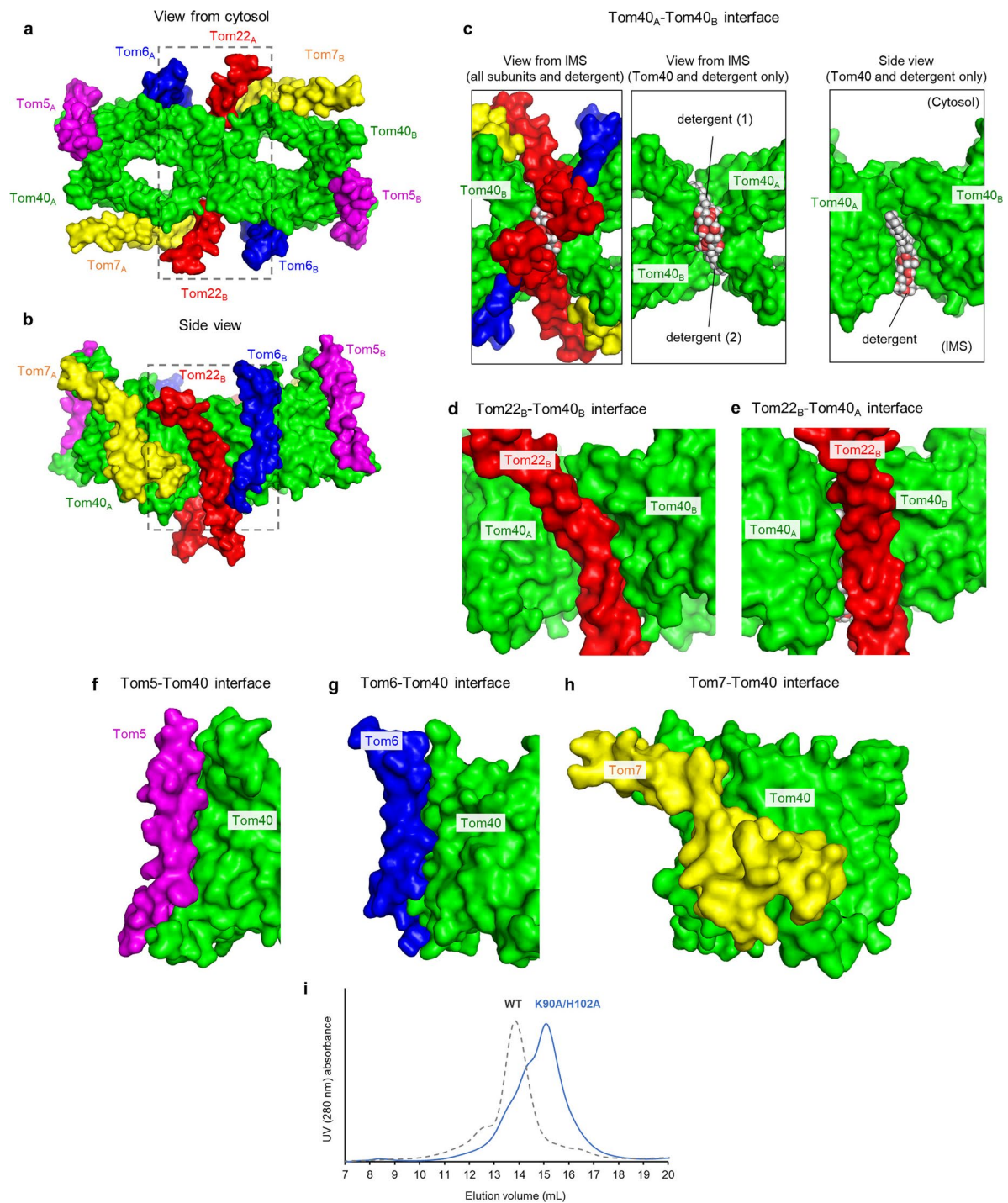
Extended Data Fig. 3 | Surface complementarity of Tom subunits at interfaces and purification of the TOM complex with a K90A H102A mutation.
**a**, **b**, Overview of the dimeric TOM complex in solvent-accessible surface representation. Shown are views from the cytosol (**a**) and along the membrane plane (**b**). The color scheme is the same as in Fig. 1. The regions marked by a dashed line are magnified in **c** (with a 180° rotation) and **d**, respectively.
c, Interface between the two Tom40 subunits. Left, a view from IMS (showing all subunits). Middle, as in the left panel but showing only Tom40 and DDM detergent molecules. Right, as in the middle panel but showing a side view. **d,e**, Side views showing the Tom40 and Tom22 interfaces within the same asymmetric unit (**d**) and between the two asymmetric units (**e**). **f**–**h**, Side view showing interfaces between Tom40 and other small Tom subunits. The viewing angles are the same as in Fig. 2b–d, respectively. **i**, Superose 6 SEC profile of the mutant TOM complex with K90A H102A Tom40 (solid blue) purified as the wild-type complex (dashed gray line; also see Fig. 1a).
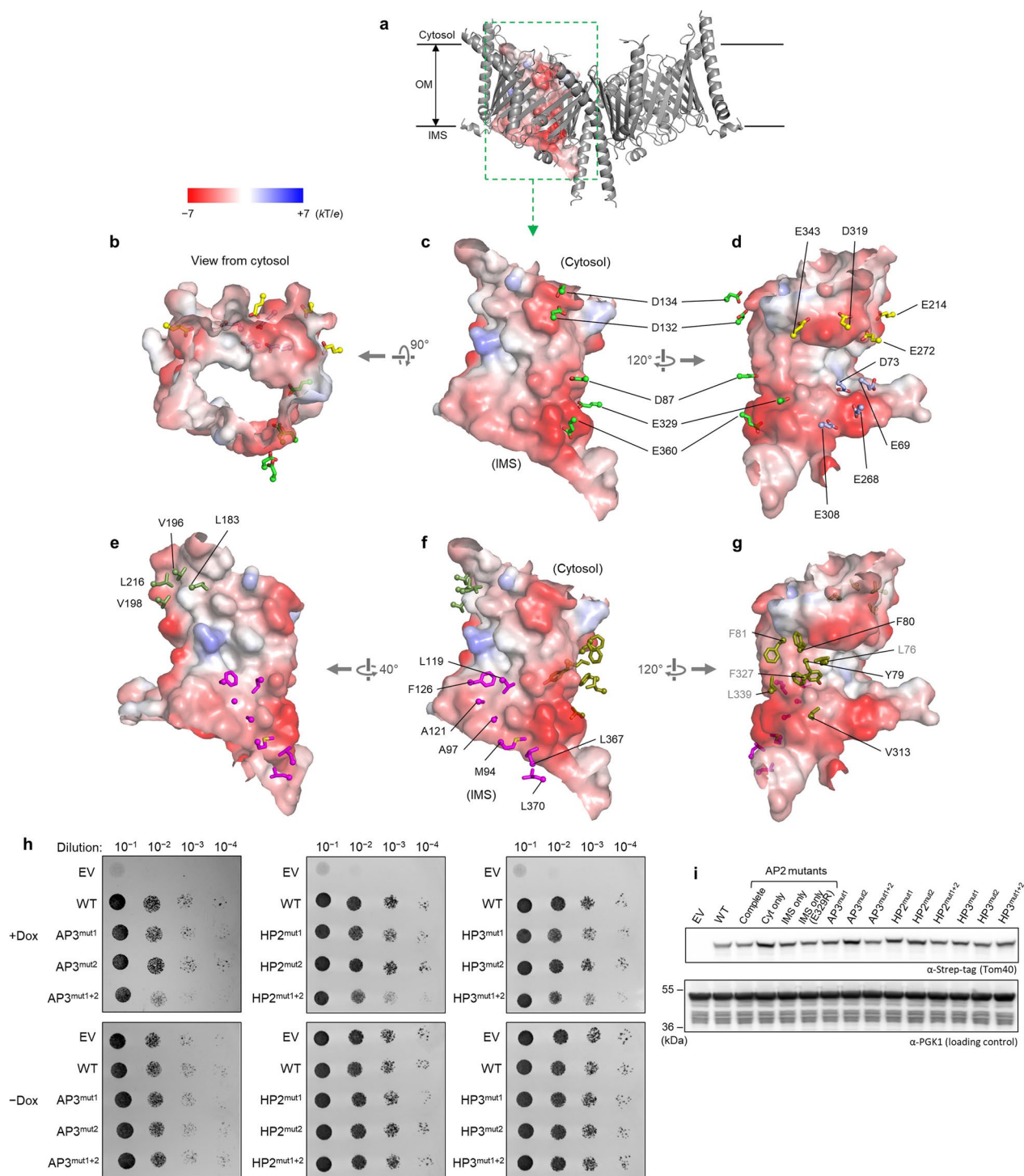
Extended Data Fig. 4 | Acidic and hydrophobic patches on the Tom40 pore surface. a, Overview (side view) of the dimeric TOM complex (gray ribbons) and the Tom40 pore cavity (surface representation; shown for only one Tom40 subunit). **b–d**, Surface electrostatics is shown as a heat map overlaid on the pore cavity shown in surface representation. Side chains of acidic amino acids are shown in stick representation (AP1, AP2, and AP3 are in yellow, green, and pale blue, respectively). In **c**, only AP2 side chains are shown for clarity. **e–g**, As in **b–d**, but side chains of hydrophobic patches are shown in stick representation (HP1, HP2, are HP3 are in olive, green, and magenta, respectively). Note that some hydrophobic side chains in HP1 (labeled in gray; F81, F327, and L76) are only partially exposed, as they are involved in interactions between the α2 segment and the β sheets. **h**, As in Fig. 3j, but with mutants of AP3, HP2, and HP3. AP3^{mut1}= E268N E308N; AP3^{mut2}= E69N D73N; HP2^{mut1}= L183S L216S; HP2^{mut2}= V196N V198S; HP3^{mut1}= L119S A121N F126N; HP3^{mut2}= M94N A97S. Dox, doxycycline. **i**, Expression of Tom40 pore mutants (contains a C-terminal Strep-tag) was examined by SDS-PAGE and immunoblotting analyses of whole-cell lysates. PGK1, loading controls. Source data for **i** are available with the paper online. The experiments in **h** and **i** were repeated at least twice with similar results.
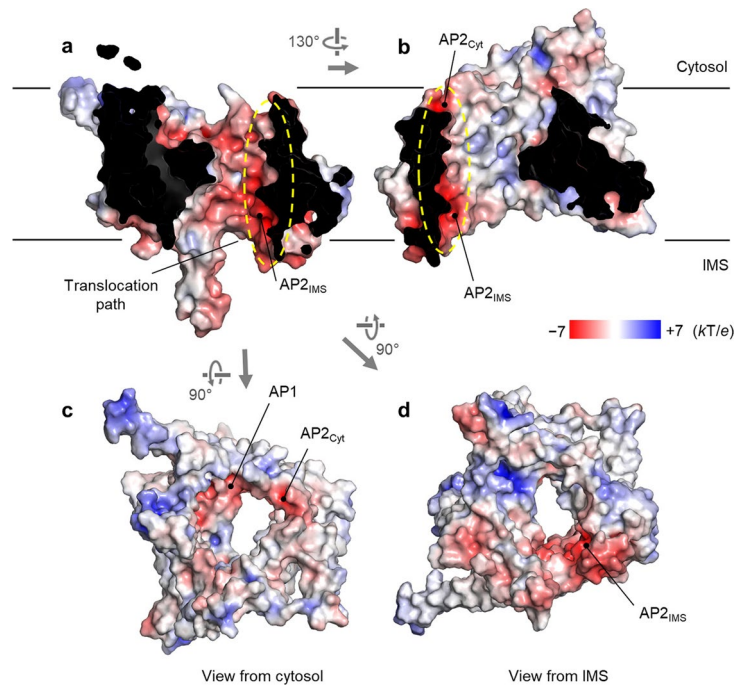
Extended Data Fig. 5 | Homology modeled pore architecture of *N. crassa* Tom40. As in Fig. 3 **a**–**d**, but with *N. crassa* TOM complex. An *N. crassa* homology model was generated by SWISS-MODEL using the *S. cerevisiae* structure as a template, and electrostatic potential was calculated by Adaptive Poisson-Boltzmann Solver (APBS). The dashed yellow line indicates AP2. Note that unlike the *S. cerevisiae* TOM complex AP3 is not prominent in *N. crassa*.
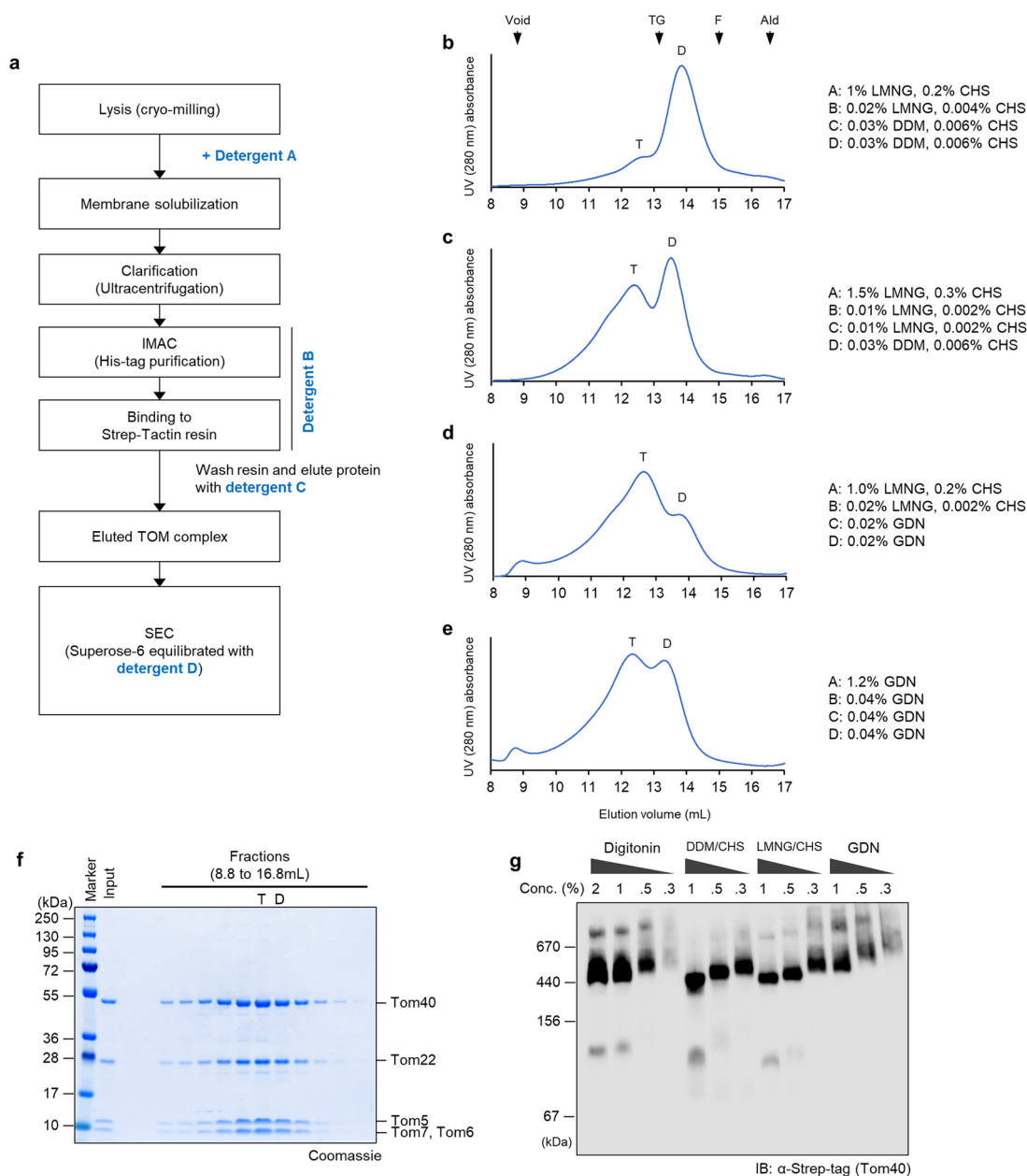
Extended Data Fig. 6 | Effects of detergent on the oligomeric state of the TOM complex. a, Schematic diagram of the TOM complex purification procedure. Different detergent conditions (indicated by blue texts) were tested (specific conditions in **b–e**). **b–e**, Detailed SEC profiles of the purified TOM complex purified under different detergent conditions. "D" indicates the dimer peak, and "T" indicates the tetramer peak. Positions of the void peak (void) and peaks of molecular weight standards are indicated by arrowheads. TG, thyroglobulin (670 kDa); F, ferritin (440 kDa); ald, aldolase (156 kDa). Note that **b–d** is the same as in Fig. 4a–c, and **b** is the same experiment shown in Fig. 1a. **f**, SDS-PAGE analysis of peak fractions from the SEC purification shown in **c**. The peak positions are marked with "T" and "D". The SDS gel was stained by Coomassie. **g**, Crude lysates prepared from cells overexpressing the TOM complex were solubilized with indicated detergent and subjected to BN-PAGE, followed by immunoblotting using an anti-Strep-tag antibody (detecting Tom40-Strep). A gradual decrease of mobility of the TOM complex accompanied by lowered detergent concentrations is likely due to an increased detergent micelle size. Source data for **g** are available with the paper online. The experiment in **g** was repeated twice with similar results.
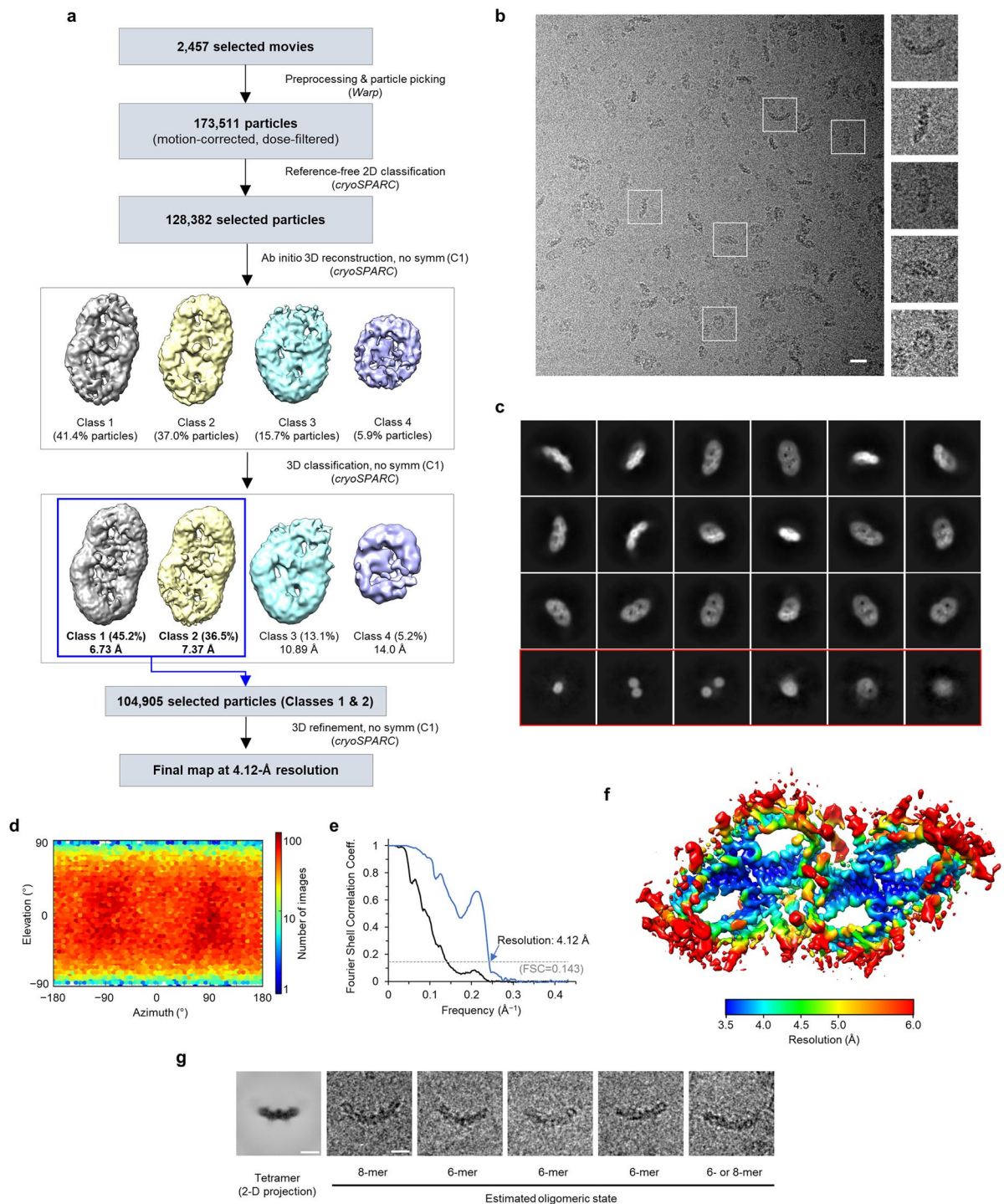
Extended Data Fig. 7 | Cryo-EM analysis of the tetrameric complex. a, Summary of single-particle image analysis procedure. **b**, A representative micrograph. Scale bar, 20 nm. The dimensions of magnified images are 414 Å (width) by 414 Å (height). **c**, Examples of selected 2D class averages. The box dimensions are 460 Å (width) by 460 Å (height). **d**, Particle orientation distribution. **e**, Fourier shell correlation (FSC). Blue line, corrected masked FSC. Solid black line, unmasked FSC. **f**, Local resolution map. **g**, Example images of particles larger than the tetramer. The leftmost image shows a 2D projection (side view with the longest width) of the 3D reconstruction of the tetrameric TOM complex. The other images show examples of large particles on micrographs. Estimated oligomeric states are indicated. Scale bar, 100 Å.
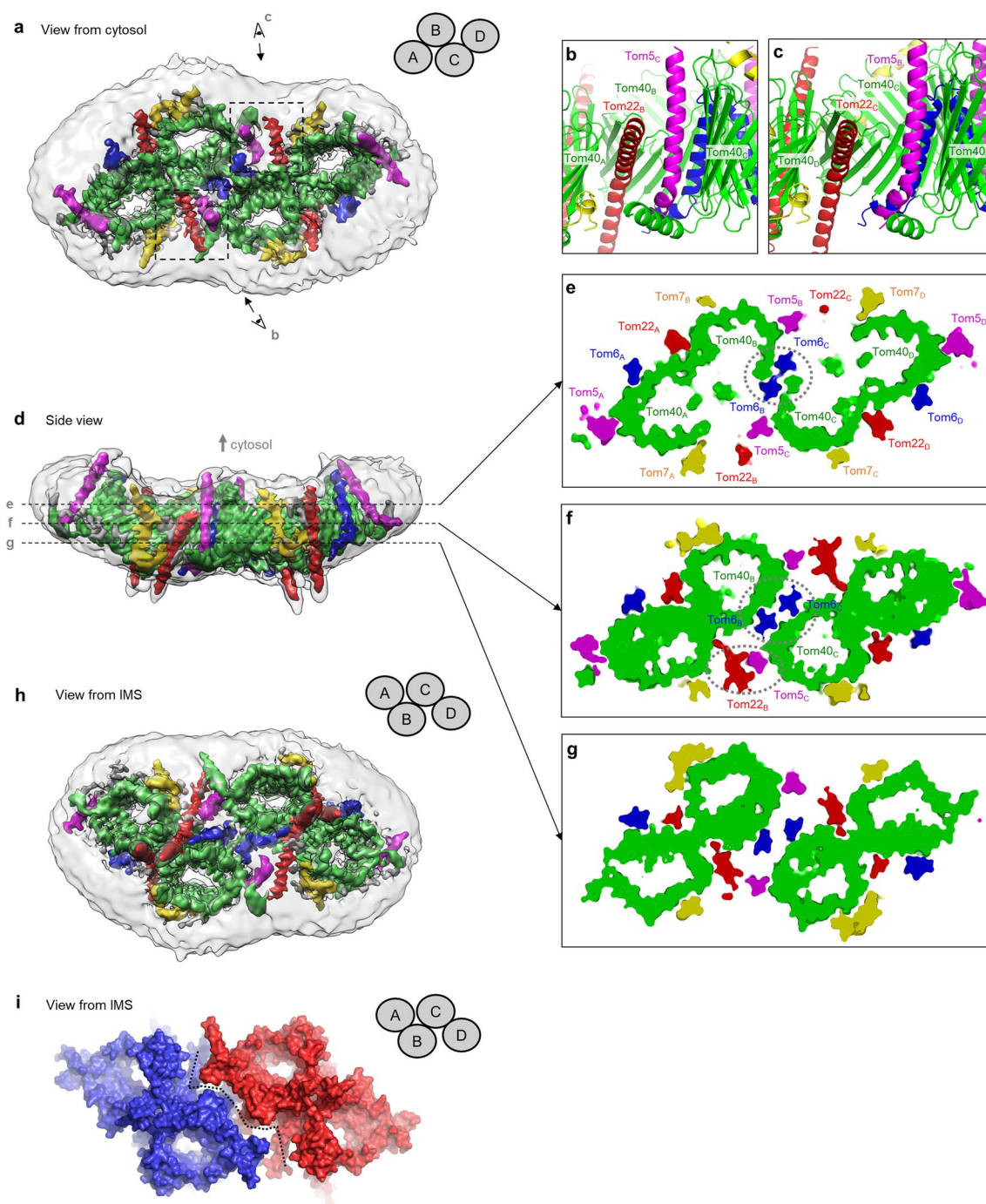
Extended Data Fig. 8 | Dimer-dimer interface in the tetrameric TOM complex. a, Overview (cytosolic view) of the tetrameric TOM complex. The 4.1-Å-resolution 3D reconstruction was represented with a composite map showing two different contour levels to show the protein features (colored contour; low-pass-filtered at 4.1 Å) and the detergent micelle (semitransparent gray contour; low-pass-filtered according to local resolution values). Organization of monomeric units are schematized in the upper right corner. Areas marked by dashed rectangles are shown in **b** and **c** (after rotating for a side view) with arrows and eye symbols indicating the viewing directions. **b,c**, Side views showing the dimer-dimer contacts between units B and C. Note that the tetramer is not symmetric and that there is a sizeable gap between Tom5$_B$ and Tom22$_C$ (**c**) in contrast to Tom5$_C$ and Tom22$_B$ (**b**). **d**, As in **a**, but showing a side view. Dashed lines indicate cross-sectional planes for cutaway views shown in **e**–**g**. **e**–**g**, Cutaway views (views from cytosol) at different positions along the membrane axis. In **e** and **f**, major interactions mediating the tetramerization are indicated by dashed ovals. Note that in **g**, there is a gap along the interface (also see **h** and **i**). **h**, As in **a** and **d**, but showing a view from IMS. **i**, Solvent-accessible surface of the tetrameric TOM complex. The dashed line indicates the interfacial gap. The two dimers (A–B and C–D) are in blue and red, respectively.
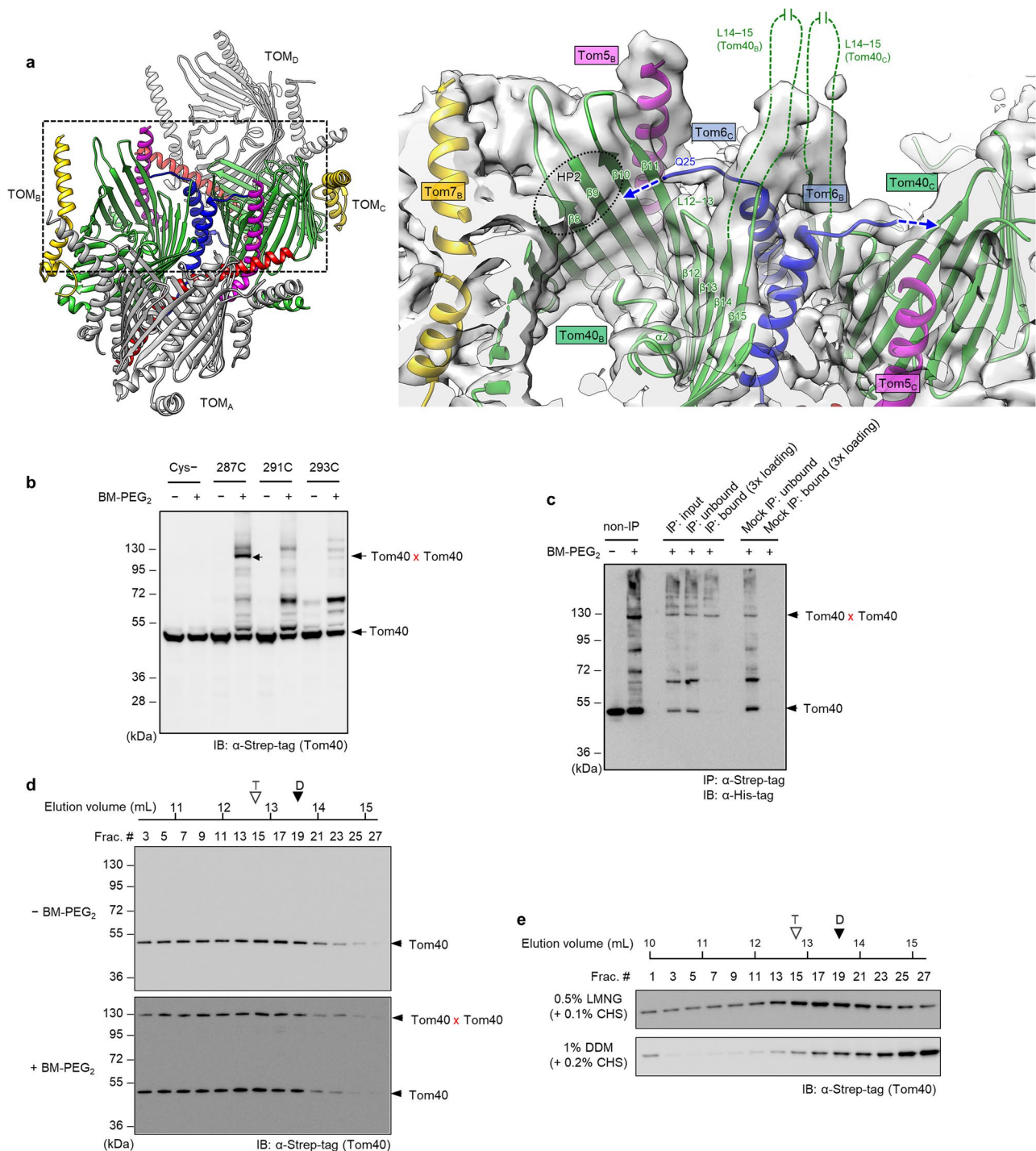
Extended Data Fig. 9 | Biochemical validation of higher oligomeric TOM complexes. a, Left, overview (angled cytosolic view) of the tetrameric TOM complex. Monomeric units B and C are shown in color, and A and D are in gray. The region in the black dashed box is magnified and shown in the right panel. Right, the cryo-EM density map (semitransparent gray) and the atomic model (in color) are shown for the B–C interface. The blue dashed arrows indicate the directions of the unmodeled N-terminal segments (residues 1–24) of the Tom6$_C$ and Tom6$_B$ subunits. The black dotted oval indicates the hydrophobic patch HP2. The green dashed lines indicate the unmodeled loop (L14-15; residues 277–294) between β14 and β15 of Tom40. **b**, Mitochondria were treated with BM-PEG$_2$ and analyzed by SDS-PAGE and immunoblotting (IB). Tom40 contained no or an indicated single cysteine. **c**, Mitochondria were purified from cells expressing Tom40$_{Strep}$ (M287C) from the chromosomal locus and Tom40$_{His}$ (M287C) from a CEN plasmid. After treating with BM-PEG$_2$, mitochondria were solubilized with octyl glucoside and subjected to immunoprecipitation (IP) using anti-Strep-tag antibodies (mock: IP without anti-Strep-tag antibodies). **d**, Mitochondria with Tom40$_{Strep}$ (M287C) expressed from the endogenous promoter were solubilized in 0.5% LMNG and 0.1% CHS and then injected to Superose 6 column. Fractions were treated with BM-PEG$_2$ before SDS-PAGE and immunoblotting. **e**, As in Fig. 4e, but with mitochondria isolated from the *tom6Δ* mutant background. "T" and "D" indicate the peak positions of tetramers and dimers, respectively. Yeast were grown in YPEG (**b** and **e**) or YPD (**c** and **d**). Source data for panels **b**–**e** are available with the paper online. The experiments in **b**–**e** were repeated at least twice with similar results.

Corresponding author(s):   Eunyong Park

Last updated by author(s):   Oct 15, 2019

Reporting Summary

Nature Research wishes to improve the reproducibility of the work that we publish. This form provides structure for consistency and transparency in reporting. For further information on Nature Research policies, see Authors & Referees and the Editorial Policy Checklist.

Statistics

For all statistical analyses, confirm that the following items are present in the figure legend, table legend, main text, or Methods section.

n/a	Confirmed	
☐	☒	The exact sample size (*n*) for each experimental group/condition, given as a discrete number and unit of measurement
☐	☒	A statement on whether measurements were taken from distinct samples or whether the same sample was measured repeatedly
☒	☐	The statistical test(s) used AND whether they are one- or two-sided *Only common tests should be described solely by name; describe more complex techniques in the Methods section.*
☒	☐	A description of all covariates tested
☒	☐	A description of any assumptions or corrections, such as tests of normality and adjustment for multiple comparisons
☒	☐	A full description of the statistical parameters including central tendency (e.g. means) or other basic estimates (e.g. regression coefficient) AND variation (e.g. standard deviation) or associated estimates of uncertainty (e.g. confidence intervals)
☒	☐	For null hypothesis testing, the test statistic (e.g. *F*, *t*, *r*) with confidence intervals, effect sizes, degrees of freedom and *P* value noted *Give P values as exact values whenever suitable.*
☒	☐	For Bayesian analysis, information on the choice of priors and Markov chain Monte Carlo settings
☒	☐	For hierarchical and complex designs, identification of the appropriate level for tests and full reporting of outcomes
☒	☐	Estimates of effect sizes (e.g. Cohen's *d*, Pearson's *r*), indicating how they were calculated

Our web collection on statistics for biologists contains articles on many of the points above.

Software and code

Policy information about availability of computer code

Data collection	For cryo-EM collection: SerialEM
Data analysis	Warp, cryoSPARC v2, CTFFIND4, RELION3, PHENIX, Coot, MotionCor2, PDB2PQR, Adaptive Poisson-Bolzmann Solver, Chimera, PyMOL

For manuscripts utilizing custom algorithms or software that are central to the research but not yet described in published literature, software must be made available to editors/reviewers. We strongly encourage code deposition in a community repository (e.g. GitHub). See the Nature Research guidelines for submitting code & software for further information.

Data

Policy information about availability of data

All manuscripts must include a data availability statement. This statement should provide the following information, where applicable:

- Accession codes, unique identifiers, or web links for publicly available datasets
- A list of figures that have associated raw data
- A description of any restrictions on data availability

The atomic coordinates of the saccharomyces cerevisiae TOM (dimer), and (tetrameric) TOM have been deposited in the Protein Data Bank under accession codes 6UCU and 6UCV respectively. The cryo-EM density maps for dimer and tetramer have been deposited in the Electron Microscopy Data Bank under the accession codes EMD-20728, EMD-20729 respectively.

Field-specific reporting

Please select the one below that is the best fit for your research. If you are not sure, read the appropriate sections before making your selection.

☒ Life sciences ☐ Behavioural & social sciences ☐ Ecological, evolutionary & environmental sciences

Life sciences study design

All studies must disclose on these points even when the disclosure is negative.

Sample size	Sample sizes were not predetermined. For cryo-EM data, sample sized were determined by availability of microscope time. Data was collected until we were able to refine a high resolution structure that enabled sufficiently accurate modeling within the confines of limited microscope time. For spot tests, we followed standard practices in the field. The growth assay contains millions of cells and we are only looking for the growth of the population of a specific yeast strain.
Data exclusions	No data was systematically excluded. The process of generating 3D maps from cryo-EM particles involves sorting for particles that are damaged, have weak signal, or that are unlikely to refine correctly. This was implemented in Warp, RELION 3.0, and cryoSPARC and is standard practice in the field.
Replication	There was no attempt to replicate cryo-EM. All biochemical experiments (yeast growth tests, crosslinking, SEC) have been replicated.
Randomization	Randomization was not attempted nor necessary this study.
Blinding	Blinding was not attempted or needed.

Reporting for specific materials, systems and methods

We require information from authors about some types of materials, experimental systems and methods used in many studies. Here, indicate whether each material, system or method listed is relevant to your study. If you are not sure if a list item applies to your research, read the appropriate section before selecting a response.

Materials & experimental systems

n/a	Involved in the study
☐	☒ Antibodies
☐	☒ Eukaryotic cell lines
☒	☐ Palaeontology
☒	☐ Animals and other organisms
☒	☐ Human research participants
☒	☐ Clinical data

Methods

n/a	Involved in the study
☒	☐ ChIP-seq
☒	☐ Flow cytometry
☒	☐ MRI-based neuroimaging

Antibodies

Antibodies used	anti-Strep-tag (Genscript; A01732), anti-His-tag (Life Technolgies MA1-21315; Proteintech HRP-66005), polyclonal anti-PGK1 (gift from J. Thorner)
Validation	Anti-Strep and anti-His antibodies are validated by the manufacturers. PGK1 antibody has been described in Baum P, Thorner J, Honig L (1978) Proc. Natl. Acad. Sci. USA 75: 4962-4966 and many other papers by J. Thorner.

Eukaryotic cell lines

Policy information about cell lines

Cell line source(s)	Common yeast strains (BY4741, YMLT62) were requested/gifted from labs per standard practice or were obtained commercially (Hughes collection,TH_7610; Dharmacon).
Authentication	Not applicable
Mycoplasma contamination	Not applicable
Commonly misidentified lines (See ICLAC register)	No commonly misidentified cell lines were used.